Computational Image Analysis Techniques for Super-resolution Localization Microscopy

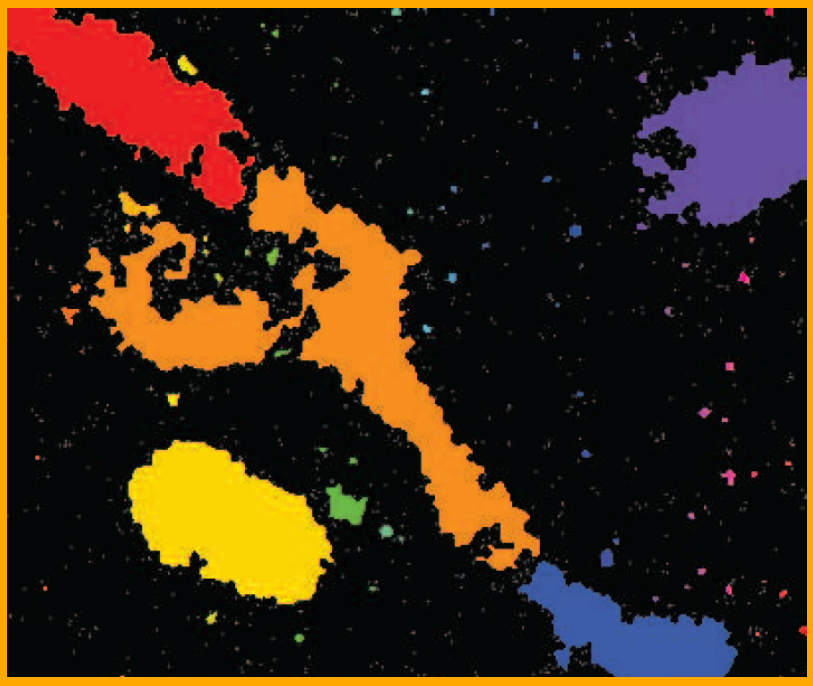

Kuan-Chieh Jackie Chen

bimagicLab
Dept. of Biomedical Engineering
Carnegie Mellon University

Computational Image Analysis Techniques for Super-resolution Localization Microscopy

Submitted in partial fulfillment of the requirements for

the degree of

Doctor of Philosophy

in

Department of Biomedical Engineering

Kuan-Chieh Jackie Chen

M.S., Electrical and Computer Engineering, Carnegie Mellon University, Pittsburgh, PA
M.S., Institute of Multimedia Engineering, National Chiao Tung University, Taiwan
B.S., Department of Computer Science, National Chiao Tung University, Taiwan

Carnegie Mellon University

Pittsburgh, PA

September 2015

Acknowledgments

This thesis concludes my five years of study at Carnegie Mellon. I have been extremely fortunate to be surrounded by many outstanding people supporting me. I could not have done anything without these supports, advisces and friendship in all aspect of my life here.

I would like to express the deepest appreciation to my adivsors, Profs. Jelena Kovačević and Ge Yang for giving me the opportunity to pursue my Ph.D. study under their supervision. Jelena, you have been my perfect role model as a leader, a working colleague, and a friend with all great enthusiasm, attitude, and dedication. You gave me the freedom and the trust to explore different ideas, experiences, research directions, and career paths that best suited to me. No matter how stressed and how dispirited I came into your office, you have always been there for me and using your m̈agic wandënlighten my feeling and turn me into positive. Your presence has always been one of my best support that have extended beyond my graduate study. I would like to thank you again for caring so much, for creating such an awesome atmosphere of our group, and for all you encouragements and life philosophy sharing. Ge, I cannot express more appreciation of your long support of me, no matter what situation I was struggled in. You have been my great example of being a researcher, a technical writer, a thinker, and a presenter. Your passion to biological research also encouraged my deep thinking of mine. You also demonstrated me that through hard work, discipline, and perseverance, anything is possible and that is exactly the right attitude a successful person should posses.

I would like to thank my committee members, Profs. José Moura, Marcel Bruchez, and Aswin Sankaranarayanan, for their time investment and their invaluable inputs as well as advices to my work. Your feedback has helped me sharpen my work and encouraged me extending my thinking direction.

I would like to thank all my labmates from both groups, Ramu Bhagavatula, Anupama Ku-

ruvilla, Mike McCann, Filipe Condessa, Siheng Chen, Rohan Varma, Anuva Kulkarni, Feng Yang, Minhua Qiu, Yiyi Yu, Hao-chih Lee, Qinle Ba, and Sahil Rastogi, for creating such a vibrant environment and for being my wonderful working colleagues, learning partners, and friends. Mike, Siheng, and Hao-chih, thank you for your constant feedback at all time. All the brainstorming sessions we had throughout years contributed every piece of this work. Yiyi, thank you for all your helps from the experimental side, which made this work possible. I enjoyed every imaging session in the lab with you.

I would like to thank my collaborators, Prof. Adam Feinberg, John Szymanski for their time working with me. John, you have been such a great working colleague and friend. We have a very good time chatting in the lab while waiting for the STORM image acquisition. I would also like to thank the rest of CBI members for all the good time we had.

Thanks to all the CMU staffs who have helped me and guided me through my study as a student. Julie Goldstein, thank you for caring about me all the time. You have been such a wonderful graduate adviser with your warm smile and hug. Christina Cowan, thank you for your smile and warm greeting every time I stopped by.

Many others also have contributed to this work in different ways, if not directly, from Pittsburgh, other cities across the states, Taiwan, and many other places. I am greatly fortunate to have them in my life to make me happy, keep me motivated and living well. To my best friends in the states: Huan-Kai Peng, Da-cheng Juan, Tsung-Hsien Lee, Weichun Lin, David Hwang, Keith Wang, Juliana Hsu, Yi-Ping Yen, Ying-Chih Wang, Maria Fang, Ian Lin, Ann Liu, Ying-Ju Yu, Mao-Lin Li, Ammon Lu, Chung-Yao Chuang, Guangshuo Liu, Jinglin Xu, Joya Deri, Lionel Levine, Alen Knapic, Cynthia Knapic, Matteus Tanha, Sonja Nakasian, Yomei Shaw, Meghan Tighe, Veronica Salazar, Yulia Zhukoff, Koichiro Suzuki. To my best friends in Taiwan: Chih-Lei Chang, Ray Chuang, Tewei Hwang, Heng Kung and Syenny Lee. Thank you all for your continued friendship throughout the years despite the geographical distance between us.

Most of all, I wish to thank my parents, my brother, and my whole family, for always being there. It goes without saying that I would not have made it here without them, especially my parents. I will forever be indebted to them for their unconditional love and support to everything in my life.

Finally, I would like to thank my funding sources, including the Philip and Marsha Dowd-ICES Fellowship from the Institute of Complex Engineered Systems at CMU, the John and Claire Bertucci

Graduate Fellowship, the National Science Foundation (through awards 1017278, DBI-1149494, DBI-1052925, and MCB-1052660), and the CMU Carnegie Institute of Technology Infrastructure Award.

Abstract

Super-resolution microscopy techniques, which overcome the diffraction limit of optical microscopy, are revolutionizing biological research by providing the ability to localize proteins within cells at nanometer resolution. Super-resolution localization microscopy (SRLM) is one of such techniques. It achieves nanometer resolution by randomly activating separate fluorophores and computationally determining their locations. While discoveries of cellular structures at nanometer resolution made recently demonstrated its potential, SRLM still faces several key technological challenges in image analysis. To overcome these challenges, we developed computational tools for analyzing and enhancing SRLM images to enable quantitative characterization and dynamic visualization of cellular processes.

One of the computational tools we developed is an image quality assessment method, which directly quantifies the accuracy or precision of the geometry or structure of the SRLM image objects. Another computational tool we developed is an SRLM image segmentation method, which identifies the boundaries of SRLM image objects by kernel density-based method. We utilize correlative fluorescence and atomic force microscopy images to characterize and validate the accuracy of the segmentation method. We have also developed a new data aggregation method under a sliding-window scheme, which improves the temporal resolution to enhance the capability of SRLM imaging of live cells. Together, these computational image analysis techniques enable fundamental extensions of SRLM, which will be essential for quantitative analysis and characterization of dynamic cellular processes.

Contents

List of Abbreviations

AC	Active Contour
AFM	Atomic Force Microscopy
AKEDS	Anisotropic Kernel Density Estimation Segmentation [1]
AS	Area Similarity
EM	Electron Microscopy
FN	Fibronectin
FPALM	Fluorescence Photoactivation Localization Microscopy [2]
FRC	Fourier Ring Correlation [3, 4]
HOG	Histogram of Oriented Gradients
IKEDS	Isotropic Kernel Desnity Estimation Segmentation [1]
KDE	Kernel Density Estimation
KS test	KolmogorovSmirnov test
PCF	Pair Correlation Function
PSF	Point Spread Function
PALM	Photo-activated Localization Microscopy [5]
SIM	Structured Illumination Microscopy [6]
STED	Stimulated Emission Depletion [7]
SRLM	Super-resolution Localization Microscopy
STORM	Stochastic Optical Reconstruction Microscopy [8]
TIRF	Total Internal Reflection Fluorescence

List of Tables

List of Figures

Chapter 1

Introduction

A fundamental aim of biology is to understand dynamic cellular processes. Direct observation of such processes using optical microscopy is the preferred approach owing to its advantages such as minimal invasiveness. However, resolution of traditional optical microscopy is restricted by the diffraction of light to ∼200 nm and ∼500 nm in lateral and axial image planes, respectively, whereas most cellular components are observable only at a scale below 100 nm. For example, folded proteins typically have a size of several nanometers, whereas cytoskeletal filaments range from ∼8 nm (actin) to ∼25 nm (microtubules) in diameter. Thus, nanometer resolution is essential for imaging how individual components assemble and function within a full cellular system. The advent of super-resolution microscopy techniques, which break the resolution limit of convention optical microscope by improving the resolution to ∼20 nm, is revolutionizing biological research with the ability to localize proteins within cells at nanometer resolution. This ability not only allows us to reveal the composition and organization of molecular complexes but also to observe intracellular dynamics in real time. Over the past decade, several novel techniques of super-resolution microscopy have been developed, for example, stimulated emission depletion (STED) [7], structure illumination microscopy (SIM) [6], as well as super-resolution localization microscopy (SRLM), such as photo-activated localization microscopy (PALM) [5] and stochastic optical reconstruction microscopy (STORM) [8]. Although these techniques are relatively new to biological research, exciting discoveries made recently have already demonstrated their capacity to provide a nanoscale view into ultrastructures. For example, recent studies of actin filaments [9] reveal a striking periodic structures of actin, spectrin, and adducin within axons of neurons (Figure 1.1A). Another

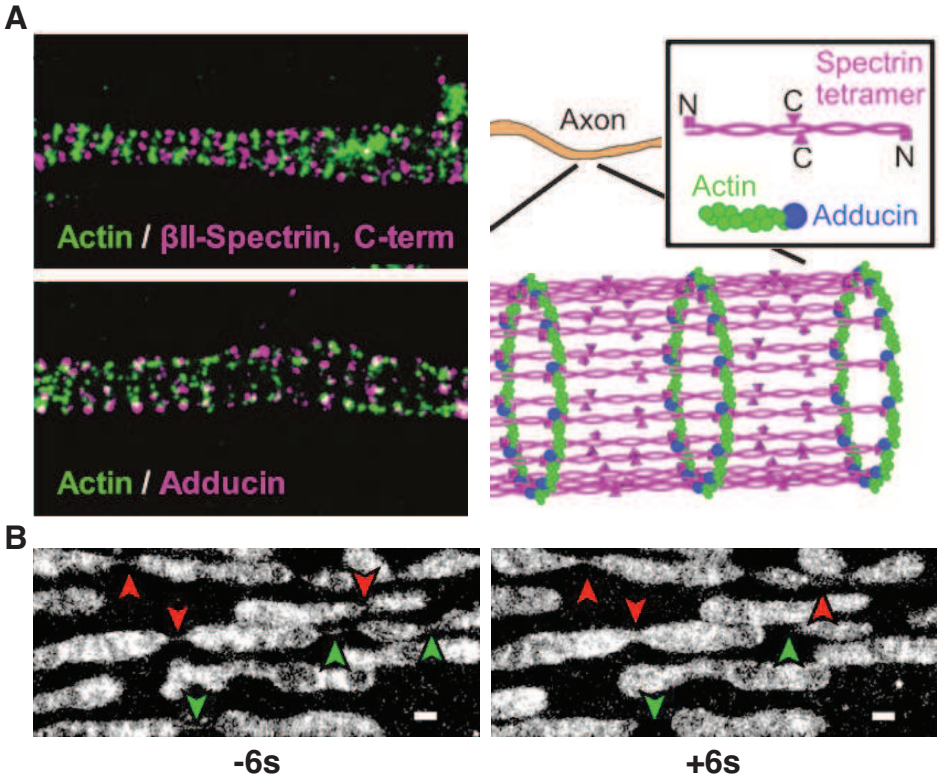

Figure 1.1: Cellular structure and dynamics revealed by STORM. (A) Periodic structures of actin filament. (B) Mitochondrial fusion (red arrowhead) and fission (green arrowhead) events captured in a time-lapse. Scale bars, 500 nm. Adapted from [9, 10] with permissions from The American Association for the Advancement of Science and PNAS.

study [10] demonstrated amazing morphological dynamics of the mitochondrial membrane during mitochondrial fusion and fission (Figure 1.1B). Other studies also demonstrated the structure of lysosomes, Golgi apparatus, nuclear pores, and focal adhesion complex [14]. These studies, which were previously infeasible using traditional optical microscopy, enable new and fundamental insights into the underlying biology.

In spite of these remarkable successes, SRLM still faces several key technological challenges in image data analysis. Currently, two fundamental challenges remain to be addressed:

1) Lack of automated computational image analysis tools. Although STORM has enabled new discoveries of biological structures and dynamics, current research is largely qualitative. SRLM images differ significantly from conventional fluorescence microscopy images because of fundamental differences in image formation. Each super-resolution image is reconstructed from a time series of images of randomly activated fluorophores that are localized at nanometer resolution and appear as clusters of particles with varying spatial densities. This thus creates a need for robust and

user-friendly image processing and data mining tools that are optimized specifically for this unique imaging modality and can provide quantitative measurements and modeling.

2) Lack of adequate temporal resolution. Beyond the static imaging analysis, more insights into biological functions depend on the ability of observing and perturbing the cellular dynamics. A fundamental limitation of current STORM imaging is that each STORM image requires a long acquisition time, which inherently limits its temporal resolution, preventing the observation of fast-changing dynamic processes in live cells.

As SRLM instruments are just becoming commercially available, biological research labs have started adopting these new imaging techniques into their study of intra-cellular processes. Currently, however, few quantitative image analysis techniques have been developed or optimized specifically for SRLM images. Moreover, limited temporal resolution remains the major shortcoming of using SRLM for observing the cellular dynamic processes from live cells.

In this thesis, we aim to present a new and substantiative departure from the status quo, namely quantitative image analysis of the SRLM images instead of the current qualitative or manual quantification analyses, which soon will become intractable especially when attempting to analyze large amount of samples. The impact of these innovations is that the tools created for improving the performance of SRLM will be useful for observing sub-cellular dynamics, and in helping biologists perform quantitative image analysis for a wide variety of biological researches.

1.1 Thesis Contributions and Outline

The main contributions of this thesis are:

1. An image quality assessment method that can quantify SRLM image information to determine whether the imaging length is sufficient to reveal the structure of imaging objects (Chapter 3, [15] and [16], in preparation);

2. A kernel density-based image segmentation algorithm that can segment structures from SRLM images(Chapter 4 and [1]); and

3. A new data aggregation method to facilitate SRLM imaging of live cells with improved temporal resolution to reveal the fast changing cellular dynamics (Chapter 5 and [17]).

The outline of the thesis is as follows. In Chapter 2, we give background information on super-resolution localization microscopy, including a literature review of the techniques applied in SRLM. Next, we present our work on SRLM image quality assessment (Chapter 3) and segmentation (Chapter 4). For SRLM imaging of live cells, we present a novel scheme of sliding-window data aggregation to improve temporal resolution (Chapter 5). We conclude in Chapter 6.

1.2 List of Publications

Reviewed journal publications.

1. K.-C. Chen, J. M. Szymanski, A. W. Feinberg, J. Kovačević, and G. Yang, "Density-based quality assessment of reconstructed images for super-resolution localization microscopy," Nature Methods, 2015, in preparation.

2. K.-C. Chen, Y. Yu, J. Kovačević, and G. Yang, "A sliding-window data aggregation method for super-resolution imaging of live cells," Optical Express 2015, in preparation.

Reviewed conference publications.

1. K.-C. Chen, Y. Yu, J. Kovačević, and G. Yang, "A sliding-window data aggregation method for super-resolution imaging of live cells," in Proc. IEEE Int. Symp. Biomed. Imag., New York, NY, Apr. 2015.

2. K.-C. Chen, G. Yang, and J. Kovačević, "Spatial density estimation based segmentation of super-resolution localization microscopy images," in Proc. IEEE Int. Conf. Image Process., Paris, France, Oct. 2014.

3. K.-C. Chen, M. Qiu, J. Kovačević, and G. Yang, "Computational image modeling for characterization and analysis of intracellular cargo transport," in Computational Modeling of Objects Presented in Images. Fundamentals, Methods, and Applications, ser. Lecture Notes in Computer Science, vol. 8641, 2014, pp. 292-303.

4. K.-C. Chen, Kovačević, and G. Yang, "Structure-based determination of imaging length for super-resolution localization microscopy," in Proc. IEEE Int. Symp. Biomed. Imag., Beijing, China, Apr. 2014, pp. 991-994.

Chapter 2

Background

In this chapter, we present background information on super-resolution localization microscopy. We describe the limitation of conventional optical microscopy and the principle of super-resolution localization microscopy and its detailed image formation process.

2.1 Fluorescence Microscopy and Diffraction Limit

Microscopy is perhaps the most important and used technique for biological research due to its capability of revealing micro-objects that are not observable by naked eye. Optical microscopy, in particular, due to its inherently non-invasive nature, is the most practical way for observing biological processes and structures in the field of cell biology. Among a wide spectrum of imaging modes in optical microscopy, fluorescence microscopy is commonly involved in cell biology research. The basic function of fluorescence microscopy is to excite the fluorescent markers that are specifically tagged to the object of interests, and then to direct the emission from markers to the detector to create signals on a dark background. This leads to high contrast and high signal-to-noise ratio compared to other modalities of conventional microscopy.

However, a fundamental limitation of conventional optical systems, including fluorescence microscopy, lies in the restriction of the resolution due to the diffraction in the objective lens. This resolution limit is defined as the required minimum distance between two ideal point sources in order to distinguish them from each other. Two values for this diffraction limit have been proposed, the Abbe and Rayleigh criteria, both related to the point spread function (PSF) [18]. The PSF

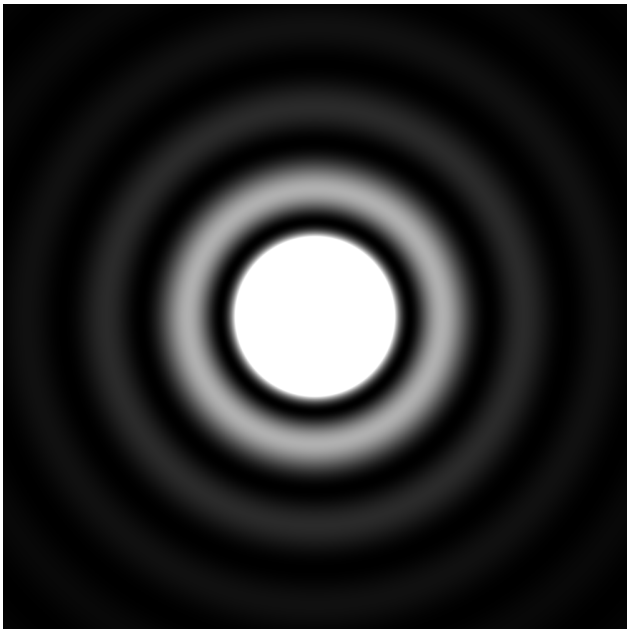

Figure 2.1: Point spread function appears as an Airy disk in the image.

represents the intensity distribution of an ideal point source of emission in the image space and shows as an Airy disk pattern in the spatial domain. In 1873, Ernst Abbe first introduced the Abbe criterion, r_{abbe}, defined as,

$$r_{\text{abbe}} = \frac{0.5\lambda}{NA} = \frac{0.5\lambda}{n\sin(\theta)},$$

where λ is the wavelength of the light source, $NA = n\sin(\theta)$ is the numeric aperture of the microscope, n is the index of refraction of the medium, and θ is the half angle of the aperture of the objective. The Rayleigh criterion, r_{rayleigh} is defined as the distance where the peak of one PSF hits the middle of the first ring of the Airy disk,

$$r_{\text{rayleigh}} = \frac{0.61\lambda}{NA} = \frac{0.61\lambda}{n\sin(\theta)}.$$

For most applications, the Rayleigh criterion is used to describe the resolution capacity of the used system.

For a typical high-end system using an oil-immersion objective with a high numerical aperture and the emission wavelength in the range of the visible light, the diffraction limit is between 200 to 250 nanometers; objects that are smaller than this can not be resolved.

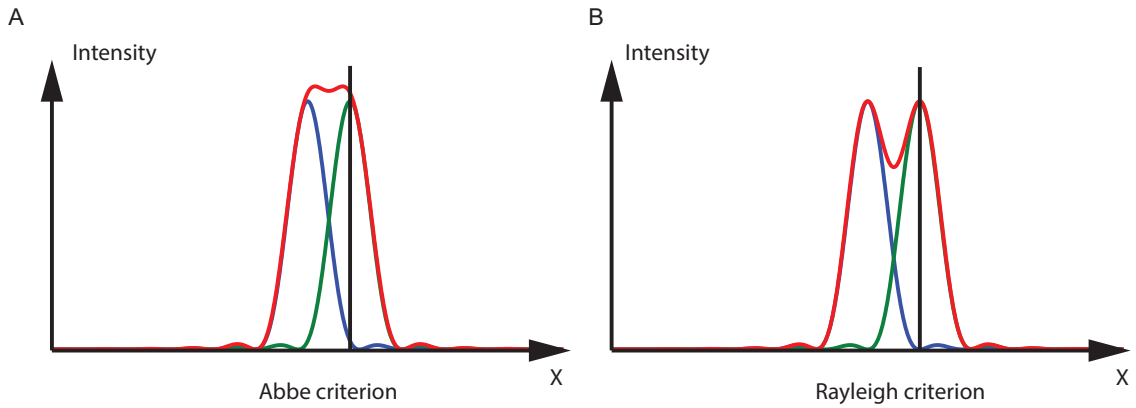

Figure 2.2: Diffraction limit, the distance between two ideal point sources of light. (A) Abbe criterion. (B) Rayleigh criterion.

There thus exists a need for a system that is capable of discerning individual molecules, which would require a resolving power greater by at least an order of magnitude.

2.2 Super-resolution Microscopy

For a long period of time, biological researchers relied on the enhanced far-field imaging system, for example, confocal microscopy or multi-photon microscopy, to obtain images with better resolution, higher contrast, and higher signal-to-noise ratio compared to traditional wide-field microscopy. However, these techniques mainly focused on improvements of the axial resolution for better optical sectioning of thick specimens, and remained restricted by diffraction limit in lateral resolution.

Alternatively, high-resolution imaging can be achieved with electron microscopy (EM), where the wavelength of the electron beam is sufficiently small to resolve nanometer-scaled molecular and even atomic-level objects. The associated photo-damaging power, however, is not acceptable for biological research, and is thus unsuitable for imaging live samples. The lack of specificity of EM also limits its application in biological research.

Recently, with the development of super-resolution microscopy techniques, new optical imaging systems have been designed that overcome the diffraction limit. There are two main categories of techniques being introduced: the patterned excitation-based and localization-based microscopy. In the former category, a patterned light illuminates the sample to modulate the emission of fluorescence, while in the second category, photo-switchable fluorescent probes are utilized to separate the emission in time. Here we describe their general principles and representative systems.

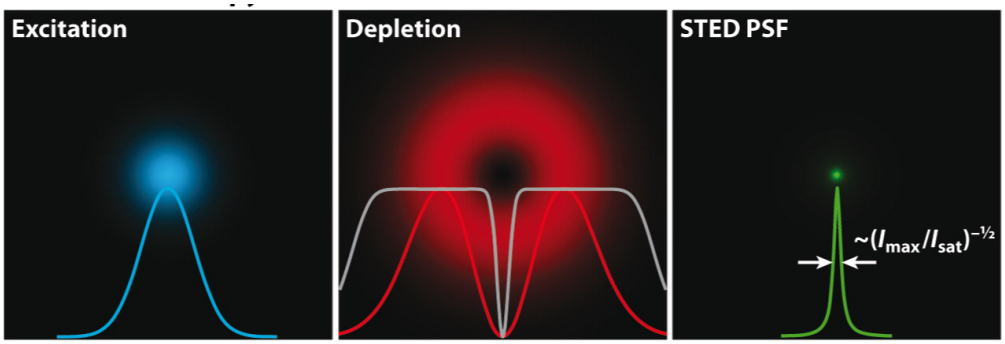

Figure 2.3: The principle of STED. Adapted from [11].

2.2.1 Patterned Excitation-based Microscopy

The idea of patterned excitation is basically to use the controlled excitation to spatially modulate the fluorescence of a subset of molecules and thus achieve sub-diffraction resolution. The most common examples are Stimulated Emission Depletion (STED) [7] and (Saturated) Structured Illumination Microscopy ((S)SIM) [6, 19].

The principle of STED is shown in Figure 2.3. It uses two excitations to create a much smaller size of PSF of fluorescence. It first excites a sample with the normal excitation light and then uses a second depletion light to force the excited molecules back to the ground state through a process called stimulated emission. The depletion light is donut-shaped so that only the surrounding molecules are being depleted, leaving only the molecules in the center emitting fluorescence and thus greatly reducing the size of the emission. Similarly to the confocal microscopy, STED then scans through the sample under such process until entire imaging region is imaged. The achieved resolution in STED is about 30-50 nm in the lateral direction.

SIM, on the other hand, uses a series of sinusoidally striped patterned excitations with different phase and angle to control the fluorescence emission, as shown in Figure 2.4. By combining these images of patterned emission, a high-resolution image can be reconstructed computationally. Typically, SIM can double the spatial resolution and thus a resolution of about 100nm in the lateral direction can be achieved.

2.2.2 Localization-based Microscopy

The second category of techniques, also called single-molecule localization imaging, uses the photo-switchable fluorescent probes, whose fluorescent state can be switched from a dark to a illumination

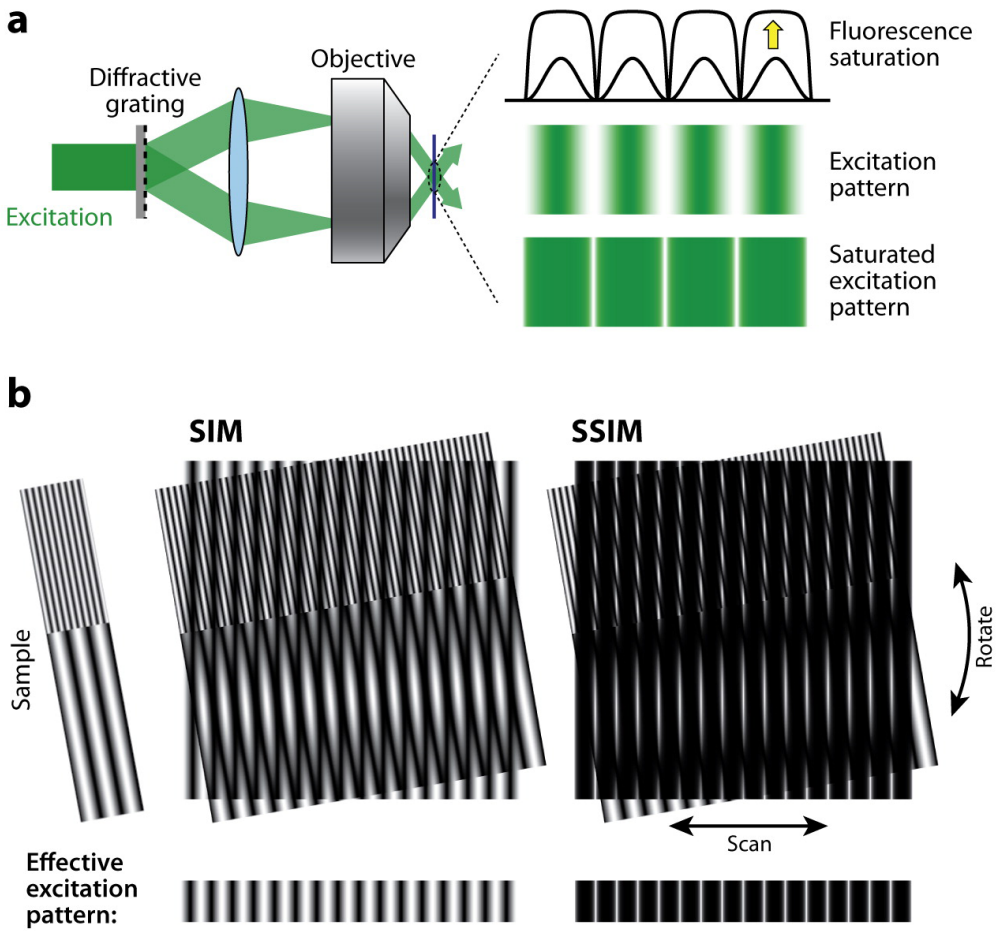

Figure 2.4: The principle of (S)SIM. (a) The generation of patterned excitation. (b) Interference of pattered excitation with sample structure to create the Moiré-effect. Adapted from [12].

state stochastically. Having only single-molecule illuminating fluorescence, these methods localize the center location of each molecule and then computationally reconstruct a high-resolution image. In 2006, three groups published similar techniques independently: These techniques have been termed Stochastic Optical Reconstruction Microscopy (STORM) [8], Photoactivated Localization Microscopy (PALM) [5], and Fluorescence Photoactivation Localization Microscopy (FPALM) [2]. A resolution of about 20-30nm has been achieved with these techniques.

2.3 Super-resolution Localization Microscopy

In this section, we review the principle and detailed process of SRLM.

2.3.1 General Principle

The idea of SRLM formed basically by combining two techniques: single-molecule localization and photo-switchable fluorescence. In early 2000s, researchers in the field of single-molecule localization enabled localizing individual sub-diffraction particles with accuracy below the diffraction limit if their PSFs do not overlap with those of the others [20]. Such techniques were initially applied in the field of single particle tracking, where the gain in resolution enabled the study of single protein dynamics. Later, with the discovery and the development of the photo-switchable fluorescence, single-molecule localization techniques extended their application into sub-diffraction imaging. Taking the advantage of photo-switchable fluorescence, the emission of each fluorophore can thus be controlled to allow only a few being imaged at a time. By performing the single-molecule localization algorithm on each raw image that contains sparsely distributed fluorophores, localized fluorophores are accumulated and the final super-resolution image is generated.

2.3.2 Fluorescence and Sample Labeling

In fluorescence microscopy, a sample labeled with fluorescent makers is illuminated with light of a specific wavelength to excite the fluorophores. Fluorophores that receive the energy from the excitation light are turned into an excited state of higher energy from the ground state. After excitation, the fluorophore will fall back to the ground state and emit the fluorescence photon with the corresponding energy difference of the transition. There is a chance that the excited fluorophore

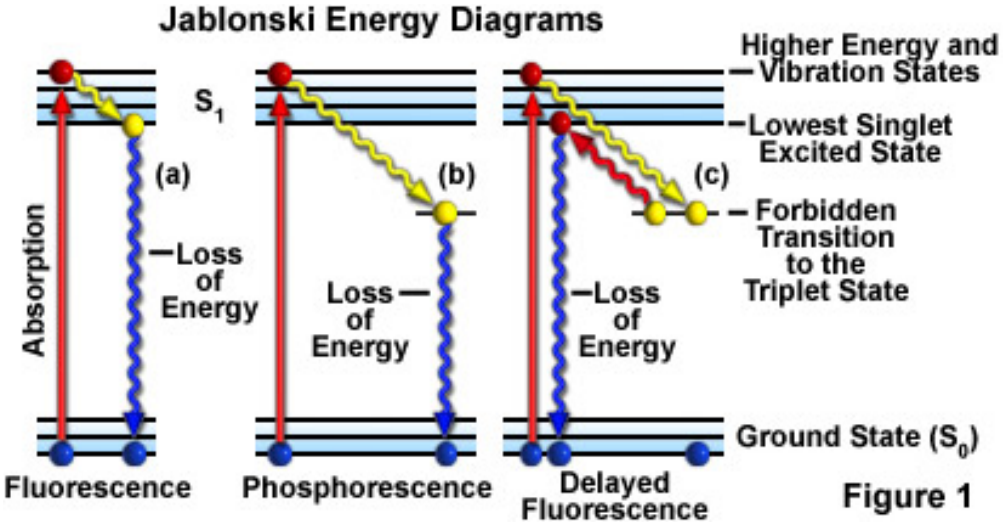

Figure 2.5: Jablonski diagram of a typical fluorophore showing excitation, fluorescence, triplet transitions. Adapted from http://micro.magnet.fsu.edu/primer/java/jablonski/lightandcolor/.

will transit into a triplet state, also called the dark-state, because these fluorophores remain dark until they return to the ground state. Figure 2.5 illustrates this process.

2.3.3 Localization

Single-molecule localization algorithms can be categorized into two types: 1) PSF fitting based methods, and 2) non-fitting based methods. For PSF fitting based methods, a common practice is to use Gaussian as the model of PSF and to fit the raw image with this model to localize the fluorophores [21]. For non-fitting based methods, many different approaches have been proposed, including radial symmetry matching based, wavelet based, compressed sensing based, etc [14,22,23]. Table 2.1 lists available algorithms and associated softwares.

Theoretical study provided analysis of how good the localization of the molecule can be achieved. In simple case, the theoretical localization precision is given by the standard error of the mean as

$$\sigma = \frac{s}{\sqrt{N}},$$

where s is the standard deviation, i.e., the width, of the PSF of the emission and N is the number of detected photons from the molecule. This represents the uncertainty when measuring the position of a molecule from the image with the detected photons of N. Based on this equation, the localization precision can be improved by either reducing the width of the PSF of the emission s or increasing

Reference	Software Name
[5]	ClearPALM
[24]	CSSTORM
[25]	DAOSTORM
[26]	FPGA Estimator
[27]	Gauss2dcirc
[28]	GPUgaussMLE
[29]	GraspJ
[30]	M2LE
[31]	Octane
[32]	PYME
[33]	QuickPALM
[34]	RadialSymmetry
[21]	RapidSTORM
[35]	ThunderSTORM
[36]	Wavelet FluoroBrancroft

Table 2.1: Localization software and their references.

the number of detected photons N. Since the s is limited by the diffraction, to localize a molecule with more precision is to improve N. Existing strategies focused on improving the emission of the fluorophore or improve the quantum efficiency of the photon detector.

Further studies of localization precision proposed more detailed estimates by taking the detector pixel size and the background noise into account. Thompson et al. [20] proposed the following equation,

$$\sigma^2 = \frac{s^2 + a^2/12}{N} + \frac{8\pi s^4 b^2}{a^2 N^2},$$

where a is the pixel size of the detector, b is the background noise, N is the detected photons, and s is the standard deviation of the PSF. Later Mortensen et al. [37] further proposed to improve the estimate by adding a factor of 16/9 into the equation and rewrote it as

$$\sigma^2 = \frac{{\sigma_a}^2}{N}\left(\frac{16}{9} + \frac{8\pi {\sigma_a}^2 b^2}{N a^2}\right),$$

where ${\sigma_a}^2 = s^2 + a^2/12$.

2.3.4 Drift Correction

As SRLM imaging requires a relatively long imaging session, it is inevitable to have sample or equipment drift caused by temperature changes or external interference. While this also occurred in conventional microscopy, which could be ignored in some cases when the drift is smaller than the resolution, it becomes unacceptable for SRLM imaging as a drift of even 10nm would completely distort the SRLM image.

In practice, two main categories of drift correction approaches have been used to address this problem: fiducial maker-based and non-fiducial maker-based approaches. For the former approach, fluorescence beads, quantum dots, and gold particles are commonly used in the preparation of the sample. As they do not blink nor bleach over the imaging session, they serve as good reference points when a post-process correction algorithm is applied to correct the drift. In non-fiducial maker-based approaches, images created by combining small batched raw image frames are compared by running image alignment algorithms to extract the drift information. Cross-correlation has been commonly used in this approach [8, 38].

2.3.5 Visualization

Unlike conventional optical microscopy, whose output is essentially the digitalized version of the light signal, the output of SRLM is a list of estimated locations of fluorophores and their uncertainties. To construct an informative image from this list, a computational method is needed.

By far, the most common visualization approach is to generate a 2D Gaussian kernel with size equal to the localization precision at each estimated fluorophore location [8] (Figure 2.6A). By taking the sum of these Gaussian kernels, a SRLM image is reconstructed. This process is essentially kernel density estimation, which gives a density map of fluorophores. Also, since the Gaussian kernel size is determined by localization precision, this process allows the precision encoded inside the image to provide a useful way to assess image quality qualitatively.

Other methods proposed to visualize SRLM data include 2D histogram (Figure 2.6B), quadtree-based adaptive histogram (Figure 2.6C), Delaunay triangulation (Figure 2.6D), and its fusion with histogram [13].

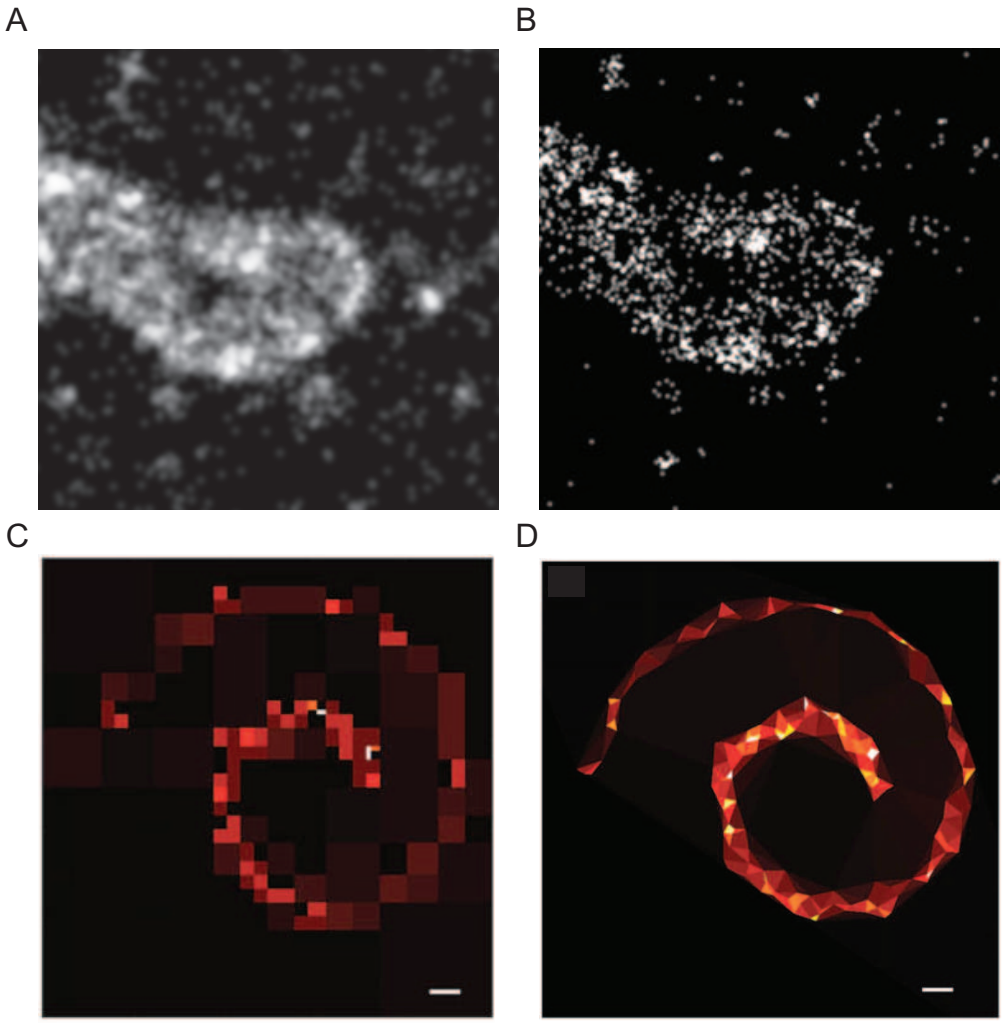

Figure 2.6: Visualization of SRLM data. (A) 2D Gaussian kernel with size equal to the localization precision at each estimated fluorophore location. (B) 2D histogram with a pre-determined bin size of 10nm. (C) Quad-tree based visualization. (D) Delaunay triangulation based visualization. Panels C and D are adapted from [13] with permission from Cambridge University Press.

2.4 Computational Methods for Localization Microscopy Image Analysis

With the introduction of SRLM instruments, recent research has started adopting these new image data to answer biological questions with various computational methods proposed to provide invaluable insight into the biological structure and cellular processes. In this section, we review two major types of analysis: molecular level analysis and intra-cellular structure level analysis [39].

Research in molecular level focused on analyzing the spatial colocalization of different types of molecules. For example, several studies proposed to use a pair-correlation function (PCF) to address molecule counting problem and simultaneously analyzing the molecule distribution [40–42]. The PCF calculates the correlation between the pair-wise distances of all localized fluorophores, which combines the true spatial correlation function and the self-correlation function caused by multiple detection of the same fluorophore. By estimating the self-correlation function from the control and then subtracting it from the experimental measurement, the true fluorophore distribution can thus be characterized.

SRLM imaging analysis of intra-cellular structure focused on the geometry information and validation. One common type is cross-section projection analysis. The spatial distribution of the image data is projected into lower dimension space where statistical analysis methods are applied for quantification [9, 10, 43, 44]. Other study also proposed to infer structures using generative models where parametric models of line or circle, for example, were used [45].

Chapter 3

Kernel Density-based Image Quality Assessment

3.1 Introduction

In SRLM techniques, each super-resolution image is reconstructed from a time series of images of randomly activated fluorophores. Here we attempt to answer the following fundamental question regarding the image reconstruction process: *how many frames of images are required to reconstruct a SRLM image of adequate quality so that it faithfully reflects the biological structures under observation?* To address this question, it is essential to have a method that directly and quantitatively assesses the quality of reconstructed images. Currently, such a method remains lacking. Instead, a commonly adopted approach is to collect a large number of frames and then assess quality of reconstructed images through visual inspection. However, this approach does not provide quantitative quality assessment, which risks acquiring either too few (not enough information) or too many (wasting time or even damaging the imaging samples by photo-toxicity) frames than needed for a given application, and thus the result is sensitive to variations among investigators making the assessment.

On the other hand, several recent studies have proposed resolution metrics, which reflects localization uncertainty and fluorophore density. A representative of these methods is Fourier ring correlation (FRC) [3, 4], which is used to determine the image resolution from the localized

fluorophore data by measuring the level of details of reconstructed images. It does not, however, directly consider the fact that images of biological structures are structured rather than random patterns. And the selection of achieved resolution remains arbitrary. Figure 3.1 shows the SRLM images reconstructed from different imaging lengths and their estimated resolutions by FRC. In particular, although at 2,000 frames, the resolution of 93nm (Figure 3.1D) is beyond the Rayleigh limit, the structure of the microtubules is not properly captured, and similarly for mitochondria (Figure 3.1B). Moreover, we found that the FRC does not give reliable resolution estimates. For example, in Figure 3.1C, the resolution estimated after 35,000 frames is higher than that at 25,000 frames, suggesting that the FRC suffers from the background noise, which can be the result of auto-fluorescence or the cross-talk signal from other channels.

In this chapter, we first developed a Gabor filter-based approach to measure the structure information. We extract this structural information using the orientation histogram with Gabor filters and perform a statistical test to determine whether information has saturated. To directly quantify the image quality, we further developed a simple kernel density estimation based technique to quantify the precision of the reconstructed geometry and structure of individual image objects. We validated the technique using correlative fluorescence and atomic force microscopy.

3.2 Methods

3.2.1 Gabor Filter-based Structure Information Measure

Problem definition

For SRLM imaging, randomly activated fluorophores from each fluorescent image are first collected. At a given imaging time t, a high-resolution image I_t is reconstructed using the detections in all frames up to time t. The goal of determining imaging length is to extract useful image information and then determine whether there is significant information change between I_t and the reconstructed image at the previous time point I_{t-1}; if not, imaging stops.

Structure-based analysis

From SRLM imaging data, we observed that the object morphology information tends to stabilize after certain imaging time. We hypothesize that by properly measuring the statistics of the contour

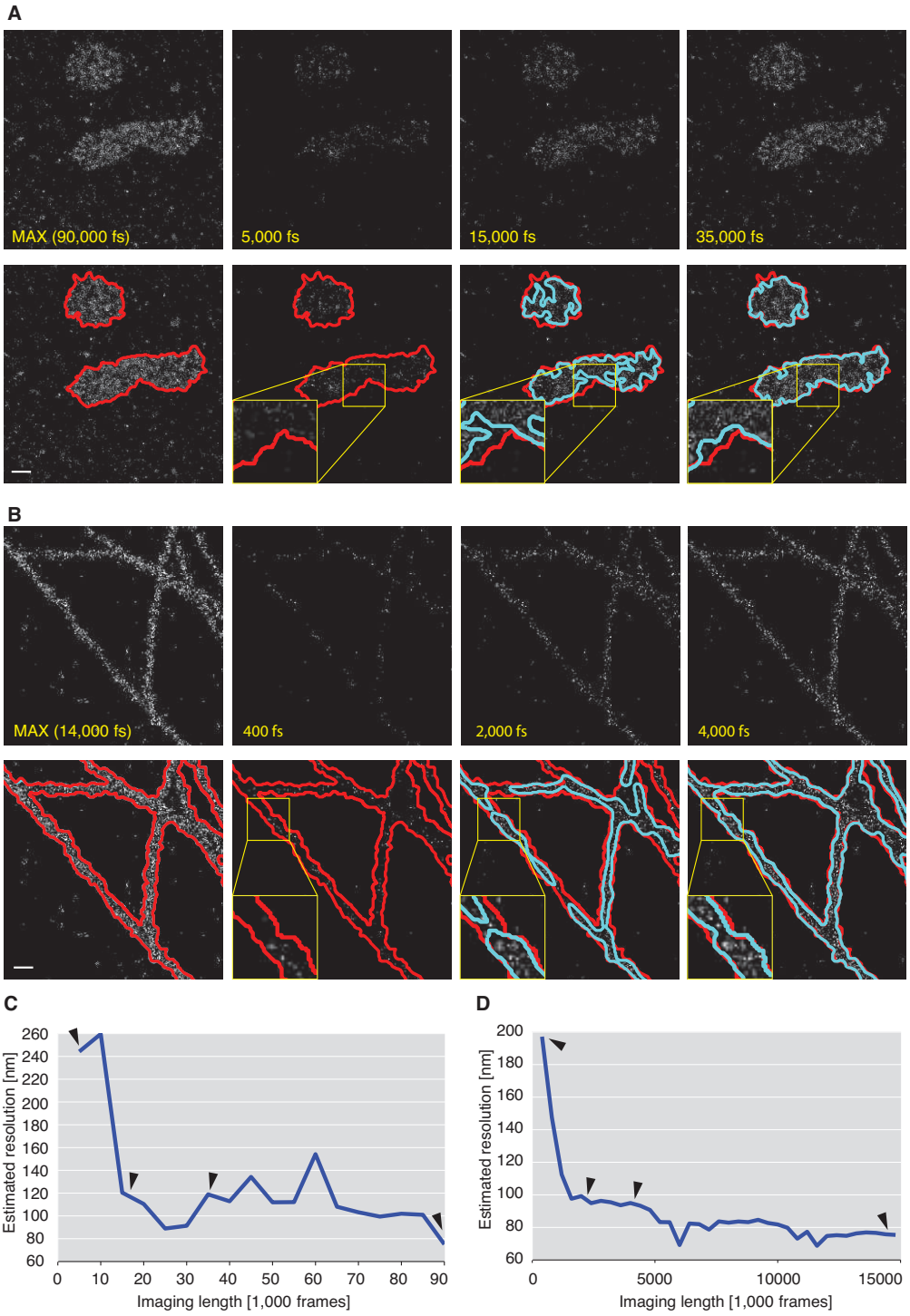

Figure 3.1: SRLM images of microtubules and mitochondria reconstructed from different numbers of images. (A) Upper row: reconstructed SRLM images of mitochondria. The number of frames used for reconstruction is shown in yellow text at the lowerleft corner. fs: frames. Lower row: segmented image objects for images shown in the upper row. Red contours show segmented image objects using all the images acquired (i.e., maximum imaging length). Cyan contours show segmented image objects within each reconstructed image. The inset is a magnified view of the yellow rectangular region. (B) Reconstructed SRLM images of microtubules. Same panel layout and color scheme as in (A). (C-D) Estimated resolutions in FRC (4) of reconstructed images of mitochondria and microtubules, respectively, at different numbers of frames, referred to as imaging lengths. Black arrowheads show estimated resolutions in FRC of the corresponding panels in column two to four of (A-B). Scale bars: 500nm.

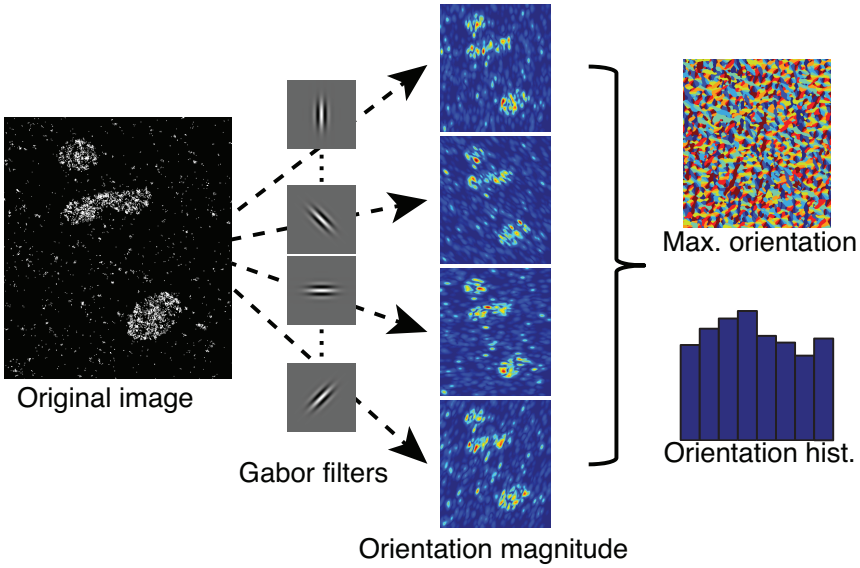

Figure 3.2: Gabor filter-based orientation histogram.

information, we should be able to determine adequate imaging length. In our preliminary experiments, we first tested the histogram of oriented gradients (HOG) features method [46], which is widely used to characterize local object appearance and morphology within an image. The HOG features are computed by taking the orientation histograms of the image gradients over dense grids of the image. Unlike natural images, however, SRLM images are mostly punctate in appearance in the foreground area (Figure 3.1A, B), and thus, taking the gradient often results in a number of local random gradient orientations instead of the structural information we aim to extract.

Inspired by the HOG features, we extend the idea of taking the orientation histogram over gradient image to taking the orientation histogram over the orientation map detected by the Gabor filters [47],

$$G_{\lambda,\theta,\psi,\sigma,\gamma}(x',y') \;=\; \exp\Big(\frac{x'^2+\gamma^2 y'^2}{\sigma^2}\Big)\exp\Big(i\Big(2\pi\frac{x'}{\lambda}+\psi\Big)\Big),$$

where $x' = x\cos\theta + y\sin\theta$, $y' = -x\sin\theta + y\cos\theta$. Each filter represents a Gaussian kernel function modulated by a complex plane wave whose wavelength and orientation are defined by λ and θ, respectively. The parameter γ specifies the spatial aspect ratio of the Gabor function, where σ is the standard deviation of the Gaussian kernel; we control it by setting $\sigma = 0.56\lambda$. We use eight different orientations, $\theta = k/8\pi$, with $k = 0, 1, \ldots, 7$, and four different scales, $\lambda = 2, 4, 6, 8$, resulting in a filter bank of 32 Gabor filters.

After convolving the image with the Gabor filter bank, the orientation histogram is obtained

by placing the maximum orientation at each pixel to the orientation bin (Figure 3.2). Specifically, let $M_\theta(x, y)$ be the filter response at orientation θ, then the maximum orientation map $\theta_{\max}(x, y)$ is

$$\theta_{\max}(x, y) \;=\; \arg\max_{\theta} \left(M_\theta(x, y)\right).$$

The orientation histogram is then obtained by voting over the entire map $\theta_{\max}(x, y)$ for each orientation as

$$h_\theta \;=\; \sum_{x,y} 1_\theta(\theta_{\max}(x, y)),$$

where $\theta = k/8\pi$, $k = 0, 1, \ldots, 7$, and $1_\theta(\tilde{\theta})$ is the indicator function that is 1 when $\tilde{\theta} = \theta$ and 0 otherwise.

Statistical imaging length criterion

At each time t, we use a statistical test to determine whether there is additional gain in terms of image information. For the proposed orientation histogram, given the histogram H_t at time t and H_{t-1} at time $t - 1$, we use the Kolmogorov–Smirnov (KS) test to determine whether H_t and H_{t-1} are from the same distribution; if so, the imaging length is considered as enough. This statistical test makes histogram-based methods more suitable for setting a global criterion than setting an arbitrary measure, for example, the distance of HOG features.

3.2.2 Kernel Density-based Geometry Information Measure

In previous section, we proposed a Gabor filter-based method for determining the imaging length. It is, however, not sufficient to directly quantify the image quality. In this section, we further develop a kernel density-based method for image quality measurement.

Estimating geometry information by density level sets

SRLM images, unlike other conventional optical microscopy images, are essentially form by clusters of detected fluorophore locations. In Chapter 4, we proposed to model such image formation as kernel density estimation. We found kernel density estimation theory developed in statistic field provides a good mathematical framework in SRLM image analysis. Specifically, suppose that the fluorescence labels of the imaging object have a certain underlying spatial distribution f, a

nonparametric density estimate of $\hat{f}_n$ based the observed fluorescence label locations $X_1, \ldots, X_n$ using a kernel density function K can be defined as

$$\hat{f}_n(X) = \frac{1}{n} \sum_{i=1}^{n} K_i(X, X_i).$$

A common practice is to choose K as an Gaussian kernel, which is defined as

$$K_i(X, X') = \frac{1}{2\pi h^2} \exp\left(-\frac{||X - X'||^2}{2h^2}\right),$$

where h is a bandwidth that controls the kernel size.

In SRLM images, an image object is fluorescently labeled such that the image object region appears as distribution with higher density. Therefore, finding the imaging object structure, i.e. boundary, can then be formulated as finding the t-level set of f, $L(t) = \{f = \tau\}$, where $\tau \geq 0$. Here the chose of t defines the threshold of the specific fluorophore density, which separates the image object region from background region.

Now, given the observed fluorescence label locations $X_1, \ldots, X_n$, the plug-in estimator of $L(t)$ is defined as

$$\hat{L_n}(\tau) = \left\{X \in \mathcal{R}^2 : \hat{f}_n(X) = \tau\right\},$$

SRLM image quality measure as boundary difference

In SRLM, randomly activated fluorophore detections from each raw image frame are first collected. At a given imaging time t, a SRLM image It is reconstructed using the detections from all frames up to time t. To estimate the image quality, we determine whether there is significant changes of boundary between the one estimated from I_t and the other estimated from I_{t1} at the previous time point.

To measure the boundary changes, a common practice is to calculate the Hausdorff distance d_{H} between two boundaries $\hat{L_1}(\tau)$ and $\hat{L_2}(\tau)$ by:

$$d_{\mathrm{H}}(\hat{L_1}(\tau), \hat{L_2}(\tau)) = \max\left(\sup_{X \in \hat{L_1}(\tau)} \inf_{Y \in \hat{L_2}(\tau)} d(X, Y), \sup_{Y \in \hat{L_2}(\tau)} \inf_{X \in \hat{L_1}(\tau)} d(X, Y)\right).$$

In SRLM, it is very common to have noise detections in the background region. To tolerant

this, we relax the sup by taking only the 95 percentage points of the distribution of d_{H} as d_{H95}.

Boundary uncertainty measure

Given the observed fluorescence label locations $X_1, \ldots, X_n$, we estimate of boundary by estimating the $L(t)$ using the plug-in estimator $\hat{L_n}(\tau)$. To understand what the uncertainty of this estimate, i.e. how well the $\hat{L_n}(\tau)$ represent the boundary of the underlying spatial distribution f of the fluorescence labels. We perform a simple bootstrap method [48, 49] to estimation the uncertainty.

Specifically, we draw a set of samples $X_1^*, \ldots, X_n^*$ at random with replacement from $X_1, \ldots, X_n$ and compute $L_n^*(\tau)$ from this set of samples. By repeating this process B times, we obtain a set of boundaries $L_{n,1}^*(\tau), \ldots, L_{n,B}^*(\tau)$. The mean boundary then can be estimated as:

$$\bar{L_n^*}(\tau) = \frac{1}{B} \sum_{b=1}^{B} L_{n,b}^*(\tau).$$

And the boundary variation for each $L_{n,b}^*(\tau)$ from mean boundary can then be estimated by calculating the 95% Hausdorff distance:

$$d_{\mathrm{H95},b}^* = d_{\mathrm{H95}}(L_{n,b}^*, \bar{L_n^*}).$$

Then, the uncertainty is estimated by finding the α percentile of $d_{\mathrm{H95},b}^*$:

$$\upsilon_{\mathrm{boot}} = d_{\mathrm{H95},B\alpha/2}^*.$$

SRLM image quality measure as internal density difference

In addition to the boundary changes, we also determine the changes of internal density distribution d_{D} between the I_t and I_{t1}. This can be done by finding the maximum density difference inside the estimated boundary. Specifically, given the observed fluorescence label locations $X_1, \ldots, X_n$, the estimated internal density $\hat{D}_n(\tau)$ is defined as

$$\hat{D_n}(\tau) = \left\{ X \in \mathcal{R}^2 : \hat{f}_n(X) \geq \tau \right\}.$$

The changes of internal density distribution thus is defined as

$$d_{\mathrm{D}}(\hat{D}_1(\tau), \hat{D}_2(\tau)) = \max\left(\hat{D}_1(\tau), \hat{D}_2(\tau)\right).$$

Similarly, we relax the max by taking only the 95 percentage points of the distribution d_{D} as d_{D95} to tolerant the noise.

3.3 Results

We performed experiments on both simulated and real SRLM images of mitochondria and microtubules.

3.3.1 Simulated Data

We simulated the molecule detections that are generated by SRLM imaging from given ground-truth samples. Two different synthetic sample structures, microtubules and mitochondria (Figure 3.3A, C), were produced to simulate common scenarios of biological structures. We assume a uniform fluorophore distribution within the structure, from which the detections of the randomly activated fluorophores are drawn with a photon count sampled from a geometric distribution. For each structure, we simulated the SRLM imaging of 200 frames, where in each frame 50 detections inside the structure area and random noise in the background area are generated (Figure 3.3B, D). This simulated imaging was divided into 20 steps, at which a high-resolution image is reconstructed by accumulating the detections starting with the first frame.

At each step, we compare the results with FRC and the structure-based measures as shown in Figure 3.3G-H. To examine how well the structure reconstructed, we used the segmentation of the underlying structure as the standard; in other words, the reconstructed image with adequate structure information should lead to good segmentation. Specifically, we segment each reconstructed image using active-mask segmentation algorithm and compare the segmentation result to the ground truth using segmentation metrics of area similarity and boundary error as shown in Figure 3.3I-J and Q-P. The performance of segmentation increases as more frames are used and saturates when the image is reconstructed with more than 50 frames.

Our method quantify the image quality by comparing the boundary difference and internal density difference between each paired steps as described in Section 3.2.2. Figure 3.3I-R summarize

the quality measures versus imaging lengths. We can see that the quality estimates match well with the segmentation result compared to the ground truth.

3.3.2 Validation Using Correlative SRLM and AFM Images

To further test the performance of the proposed measure, we developed correlative SRLM and AFM.

STORM imaging setup

For the STORM imaging, we used a Nikon N-STORM system equipped with a motorized XY stage and a Nikon perfect focus system. A monolithic laser combiner (Agilend MLC400) was controlled by the computer. The laser passed through a TIRF system and focused to the back focal plane of the oil-immersion objective (Nikon APO 100x/1.4). For the excitation, the power of 647nm (Alexa Fluor 647) laser was 90mW/cm^2 measured at the objective. The emission signal from the excited fluorophores was detected by a EMCCD camera (Andor iXon Ultra 897). The effective camera pixel size under 100x objective was 156nm. All instrument control and image acquisition were performed with Nikon NIS-Elements software package.

Atomic force microscopy imaging of immobilized fibronectin fibers

AFM (MFP3D-Bio, Asylum Research) was used to provide the ground truth dimensions of the Fibronectin (FN) fibers imaged using STORM. After STORM imaging, the FN fibers were rinsed 3x with distilled water and dried in an oven at 37°C. Once dry, the FN fibers were scanned in air using AC mode with AC160TS-R3 cantilevers (Olympus Corporation). High-resolution AFM images were obtained using 2580 points and lines over a scan area of 30 μm x 30 μm. The raw data from the AFM height signal was then exported into MATLAB for further processing.

STORM and AFM image alignment

For new microscopy development, correlative microscopy has been served as an important tool for validation. For STORM, this is particularly crucial as STORM image is a reconstruct from clusters of fluorophore detections that are sparsely distributed in imaging region and thus require a different microscopy image modality for validation. STORM and AFM images are completely different image

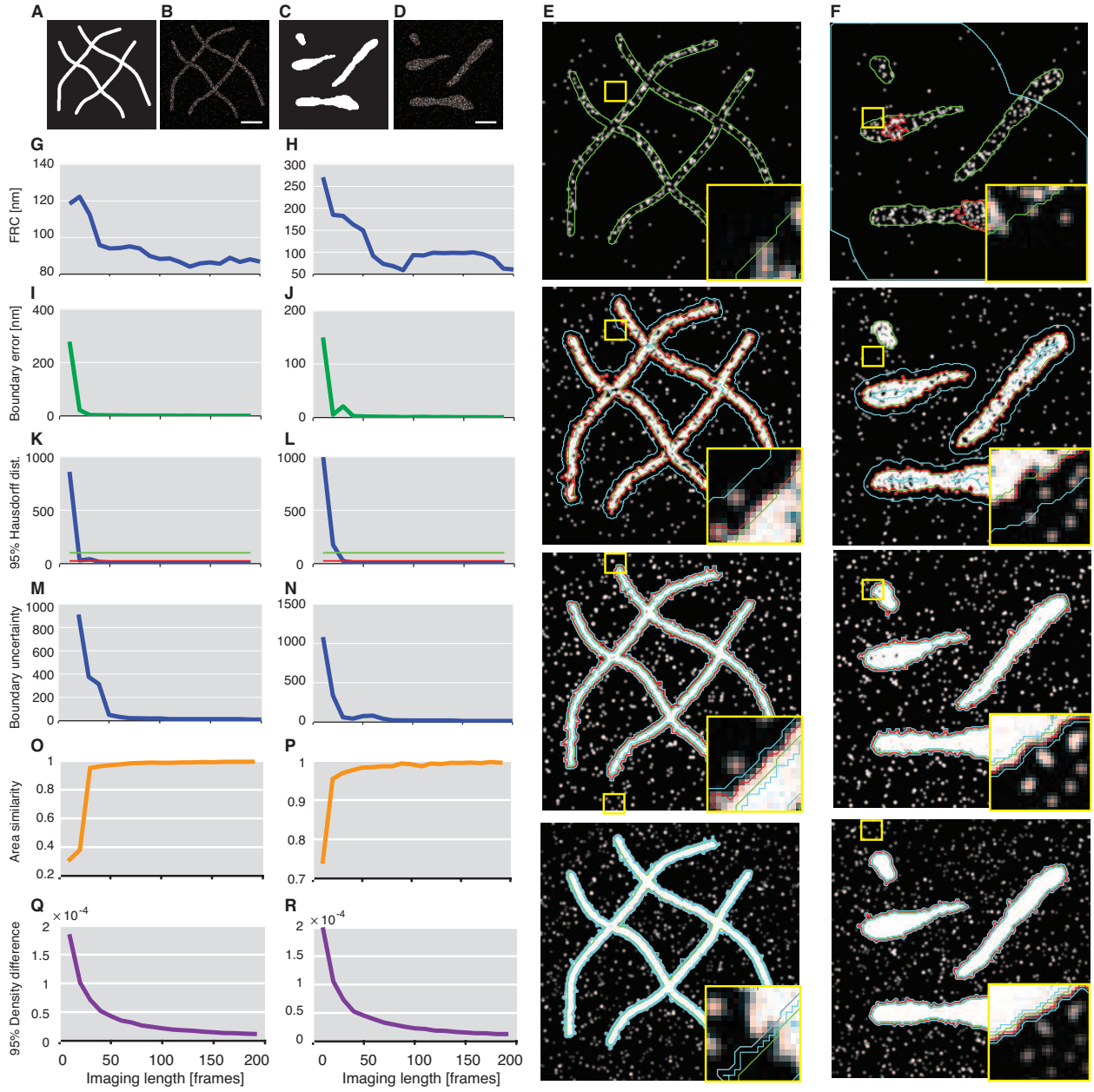

Figure 3.3: Demonstration of density-based assessment method on simulated data. (A-B) The ground truth image (A) and a reconstructed SRLM image (B) of a microtubule network. (C-D) The ground truth image (C) and a reconstructed SRLM image (D) of a group of mitochondria. (E-F) Reconstructed images from different numbers of images. Green contour: ground truth boundary. Red contour: current mean boundary. Cyan contour: boundary uncertainty band. Inset at the lower right corner of each image is a magnified view of the small region enclosed by the yellow rectangle. (G-R) Characterization of quality of reconstructed images using different metrics, including: (G-H) FRC, (I-J) boundary error compared to ground truth, (K-L) 95% Hausdorff distances between each pairwise steps (the red and green horizontal lines represent the 25nm and 100nm), (M-N) boundary uncertainty, (O-P) area similarity compared to ground truth, (Q-R) 95% density differences between pairwise steps. Left column: microtubule. Right column: mitochondria. Scale bars, 500nm.

modalities where STORM image is formed by a cluster of fluorophore detections sparsely distributed in imaging object region and AFM image is formed by dense grid height measurements of imaging objects surface. Since the fibronectin fibers are immobilized, we adopted multimodal intensity based rigid-body image registration method to align these two images. The transformation model used here only includes spatial translation and rotation. Mattes mutual information metric [50] with histogram of 100 bins is used as the similarity metric. We implemented this algorithm using MATLAB image processing toolbox.

Results

Figure 3.4 summarizes the results of the proposed methods validated by correlative SRLM and AFM images. We can see that the estimates of both boundary and internal density changes matches well with the segmentation results compared with AFM images, demonstrating that the proposed method can directly quantify both the geometry information.

3.4 Summary

In this chapter, we presented a kernel density-based approach to directly quantify the image quality for SRLM. The method uses the density distribution estimated by plug-in estimator to measure the image quality which represents amount of information in the image. Compared to methods based entirely on image resolution, our method provides a reliable way of measuring imaging quality. Because of the incorporation of density estimation of the fluorophores, this method is particularly well suited to applications that involve subsequent computational image analysis. The proposed approach does not depend on specific image structure and can thus be used in a broad range of biological applications of super-resolution imaging.

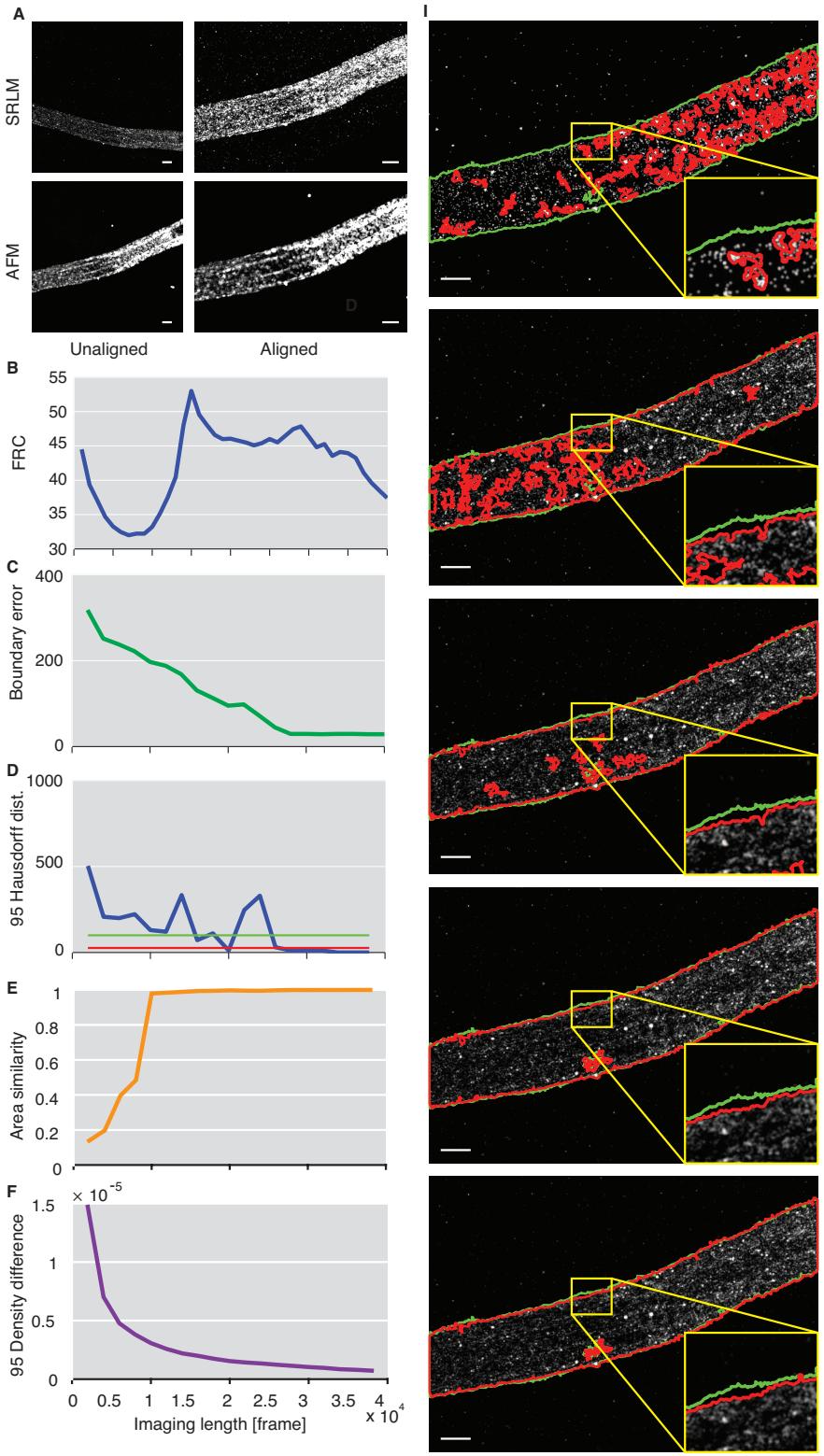

Figure 3.4: Demonstration/application of density-based quality assessment on actual experimental data using correlated SRLM and AFM. (A) Unaligned SRLM (Top-left panel) and AFM (Bottom-left panel) images of a fibronectin bundle as well as their corresponding images after alignment (Top-right and bottom-right, respectively). Scale bars: 1 um. (B-F) Characterization of quality of reconstructed images using different metrics, including FRC (B), boundary error (C), 95% Hausdorff distance between boundaries (D), area similarity (E), and 95% density difference (F). (I) Reconstructed SRLM images from different numbers of images. Green: ground-truth provided by AFM. Red: segmentation of reconstructed image. Inset at the lower right corner of each image is a magnified view of the small region enclosed by the yellow rectangle. Scale bars: 1 um.

Chapter 4

Kernel Density-based Image Segmentation

In general, image segmentation is the task of dividing an image into regions of similarity. For biological images, the main task is to segment the cellular or subcellular structures from background. However, as noted previously, SRLM images differ significantly from conventional fluorescence microscopy images because of fundamental differences in image formation. Each SRLM image is reconstructed from a time series of images of randomly activated fluorophores and represented by clusters of particles, localized at nanometer resolution, of varying spatial densities. Currently, however, few quantitative image analysis techniques exist or have been developed or optimized specifically for SRLM images, which significantly limit accurate and reliable image analysis. This is especially the case for image segmentation, an essential operation for image analysis and understanding. In this chapter, we propose to address the problem of SRLM image segmentation by developing a statistical method based on estimating and smoothing spatial densities of fluorophores in SRLM images, from which we can derive segmentation algorithm.

4.1 Introduction

Image segmentation is often the first step in quantitative image analysis. Although super-resolution images provide significantly improved spatial resolution in visualizing cellular structures (Fig. 4.1), this improvement in SRLM image analysis can only be achieved using reliable and accurate image

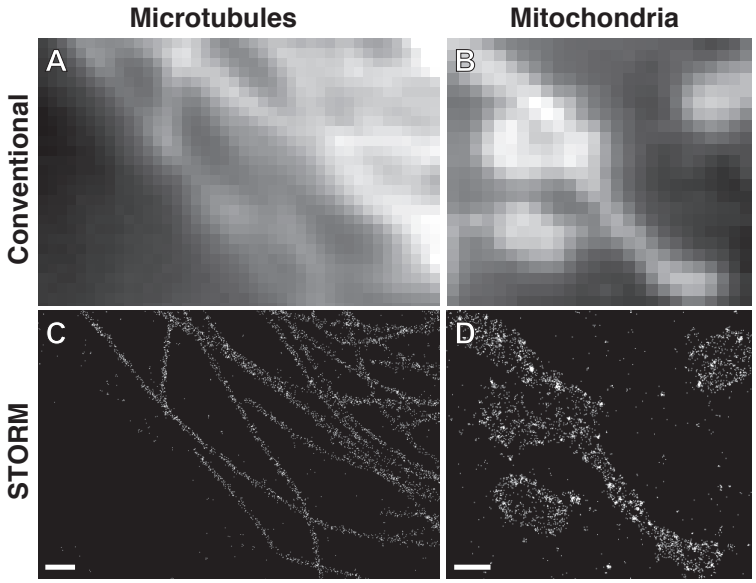

Figure 4.1: Comparisons between conventional fluorescence microscopy and STORM images of microtubules and mitochondria. (A, C) Widefield and STORM images of microtubules, respectively; (B, D) widefield and STORM images of mitochondria, respectively. Scale bars, 500nm.

segmentation tools. In the past decades, there exists a wide variety of classic approaches for biological image segmentation, including graph cuts [51], active contours [52], level sets [53, 54], active masks [55]. From our preliminary experiments, these existing methods have difficulties segmenting objects in SRLM images due to a complete different image formation compared to conventional microscopy images that these methods were originally designed for.

In conventional epifluorescence or confocal microscopy images, objects can generally be characterized as continuous regions of fluorescence signals. In contrast, objects in SRLM images appear as clusters of estimated fluorophore locations with different spatial densities. To visualize detected fluorophores, common approaches are to render each particle as a normalized Gaussian kernel with the size proportional to the localization precision or to render a spatial histogram with a prespecified bin size [13]. Direct segmentation of such images using existing methods is problematic. As shown for example in Fig. 4.1, SRLM images appear punctate and the edges of image objects are often poorly defined due to random activation of fluorophores. Essentially, the randomly activated fluorophores provide a sampling of the underlying true spatial density distribution of all fluorophores.

Another commonly encountered issue in SRLM images is sparsely distributed artifacts (particles) appearing in the background regions, which may result from diffused fluorophores; these

isolated features need to be properly addressed in image processing to avoid false segmentation. In general, reliable and accurate segmentation of SRLM images must take into account the unique properties of such images. An intuitive strategy is to estimate the underlying spatial density according to the sampled spatial distribution of the particles and then determine the criterion for segmenting the density image.

In this chapter, we propose a spatially adaptive density estimation based method for smoothing and segmenting SRLM images. We propose to estimate local particle density using anisotropic kernels that adapt to local particle distributions. This kernel based method provides a way to connect separated particles in an object region as well as to interpolate object boundary without being misled by the random fluctuations of activated boundary fluorophores.

4.2 Methods

4.2.1 Problem Formulation

To take into account the unique modality of SRLM images, we formulate the image segmentation problem as identifying high density foreground regions from low density background. We propose a two-step process for SRLM image segmentation: 1) spatial density distribution estimation and 2) image segmentation based on thresholding that estimated density distribution. In our preliminary experiments based on previous work on density estimation [56], we first tested spatial density estimator using commonly adopted kernel density estimator.

4.2.2 Density Estimation with Histogram

The simplest density estimators are perhaps histograms. A spatial histogram is constructed by dividing the 2D space into equal sub-tiles as bins and counting the number of points that fall inside region of each bin. Specifically, suppose that we have a list of n points $x_1, x_2, \ldots, x_n$ in the image region A. Divide A into N bins $B_1, B_2, \ldots, B_N$ of size h^2. Then the density for each bin is

$$\hat{f}(B_j) = \frac{1}{h^2} \sum_{i=1}^{n} I(x_i \in B_j).$$

4.2.3 Density Estimation with Isotropic Kernels

A commonly used density estimation is the kernel density estimator. The idea is to estimate a continuous distribution from a finite set of points by placing a kernel centered at each points and taking the sum of all kernels. Kernel density estimation has been used previously in applications such as geographical information systems [57].

Specifically, suppose that we have a list of n points $x_1, x_2, \ldots, x_n$, sampled from some unknown density map f of a spatial area (in our application, the image). A classic 2D spatial kernel density estimator at location x is

$$\hat{f}(x) = \frac{1}{n} \sum_{i=1}^{n} K_h(x, x_i), \tag{4.1}$$

where K_h is a symmetric isotropic kernel function. A commonly used kernel function is the Gaussian kernel, which is defined as

$$K_h(x, x') = \frac{1}{2\pi h^2} \exp\left(-\frac{||x - x'||^2}{2h^2}\right),$$

where h is a global spherical bandwidth, which can be estimated from the data by minimizing the L_2 risk function using cross-validation [56]. However, in SRLM images, h directly controls the resolution of the estimated density image as it represents the radius of the point-spread function of the density image. If the h is too small, the density estimator loses its power to connect the particles; if h is too large, the resolution degrades. Because the typical range of resolution for SRLM is $20 \sim 100$ nm, we choose h to be in the range of $10 \sim 50$ nm, i.e. half the resolution.

4.2.4 Density Estimation with Adaptive Anisotropic Kernels

The main limitation of the isotropic kernel appears when it is placed at a location where the support of the underlying true density is close to one dimensional (for example, on the boundary). Isotropic kernel cannot properly represents the heterogeneity of the spatial density; it, instead, spreads its density mass equally along all spatial directions, thus, giving too much emphasis to background regions and too little along the boundary direction. This motivates us to use adaptive, anisotropic kernels for density estimation.

The adaptive anisotropic kernel density estimation associates with each point an anisotropic kernel. This kernel adapts to the local structure of the data points by estimating locally its scale,

shape, and orientation. Again, the density function as in (4.1) at the location x is a sum of kernels centered at the surrounding points x_i where now each kernel $K_i(x, x_i)$ is the locally adaptive anisotropic Gaussian kernel

$$K_i(x, x_i) = \frac{1}{2\pi|\Sigma_i|} \exp\left(-\frac{1}{2}(x - x_i)^\top \Sigma_i^{-1}(x - x_i)\right),$$

where Σ_i is a positive definite covariance matrix that defines its configuration (scale, shape, and orientation).

To place the anisotropic kernel according to the spatial distribution of local data points, for the kernel located at the point x_i, we select its k-nearest neighbors x_1, $x_2, \ldots, x_k$, to estimate the covariance matrix

$$\Sigma_i = \sum_{j=1}^{k} (x_i - x_j)(x_i - x_j)^\top.$$

Here k must be at least $d + 1$ to get the support of Σ_i, where $d = 2$ is the spatial dimension. The size of the anisotropic kernel is controlled by the distance between x_k and x_i. Choosing a larger k helps to better estimate the distribution of local points; we must guard against too large a k, however, to prevent the resolution degradation. We propose to evaluate sensitivity of the density estimation to k to provide a general suggestion of the choice of k .

Fig. 4.2 demonstrates the qualitative differences between the density estimations using isotropic kernel and adaptive anisotropic kernel. Estimating from the points sampled from two structures, the isotropic kernel yields a fair density estimation for both structures but generally spreads out the regions, making the region much bigger than the distribution of the points. In contrast, the adaptive anisotropic kernel follows the local distribution of the points and yields a density estimation with more precise boundaries compared to the one from the isotropic kernel.

4.2.5 Density Threshold Determination

The estimated spatial density distribution provides a way of smoothing the SRLM images. We now need to determine a criterion to segment the regions with different density statistics. In our preliminary work, we begin with simple strategy: global thresholding. Assuming two types of signals: signals of the actual fluorophores and background signals, we can empirically model the density distribution of the foreground regions obtained by finding the nonzero density bins from the

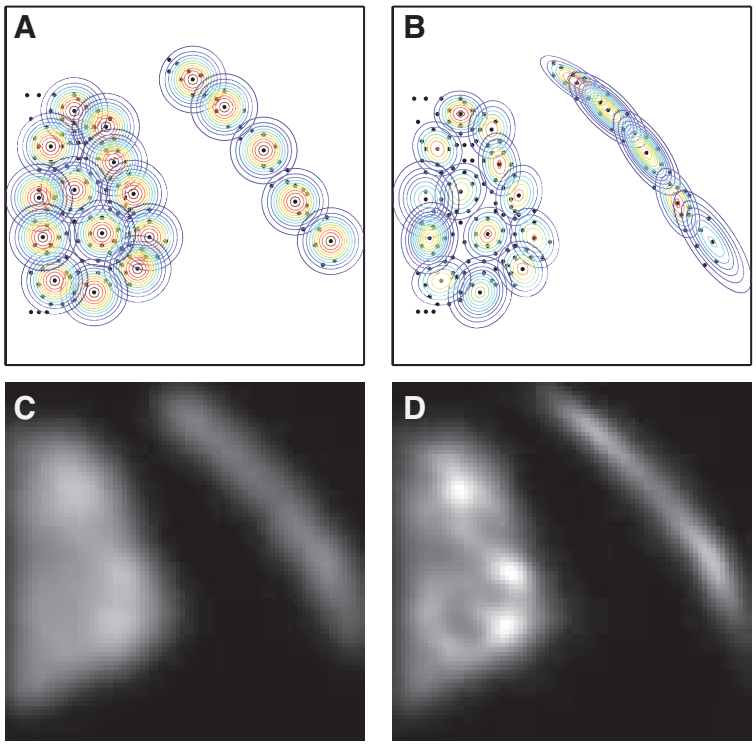

Figure 4.2: Isotropic vs adaptive anisotropic kernels. Selected isotropic kernels (A) and adaptive anisotropic kernels (B) overlapped on the data points sampled from a curvilinear and a big blob structures. Estimated density images using isotropic kernels (C) and adaptive anisotropic kernels (D).

spatial histogram. The thresholding can then be set by finding the pth percentile of the densities to find the best segmentation.

From the preliminary results [1], the global thresholding demonstrate the effectiveness of the adaptive spatial density estimation. However, this method is based on the assumption of the presence of only two types of density distributions, which may not be always true for real applications. For example, the spatial distribution of fluorophores may not be the same for all cellular objects, leading to the need to determine a segmentation criterion that incorporates these factors. We plan to extend the thresholding to adaptive one determined by local statistical analysis of the estimated density distribution.

4.3 Results

We performed experiments on both simulated and real SRLM images of mitochondria and microtubules. The segmentation performance of the Chan-Vese active contour (AC) [53], the isotopic kernel density estimation based segmentation (IKDES), and the proposed adaptive anisotropic kernel density estimation based segmentation (AKDES) algorithms were compared qualitatively and quantitatively using both simulated and real SRLM images.

4.3.1 Simulated Data

We generated SRLM images of random fluorophore activation from given ground-truth. Two types of synthetic sample structures, microtubules and mitochondria, were produced to simulate common biological structures. Assuming a uniform fluorophore density in the object regions, we generated the detections of the activated fluorophores randomly with two different labeling densities of 1,000 and 2,000 detections in an image region of 2560×2560 nm, and added random artifacts in the background area with four different signal to artifact ratios of 5, 10, 20, and 40 dB.

Fig. 4.3 shows a qualitative comparison of the three segmentation algorithms. As previously noted, the AC method performed poorly on SRLM images. It was sensitive to local missing particle regions inside the object owing to the random fluctuations of the activated fluorophores in SRLM images. On the other hand, the IKDES method connected the region better but still suffered from over-segmentation and the false segmentation of the background artifacts. In contrast, the proposed AKDES method outperformed the other two methods in more precisely following the

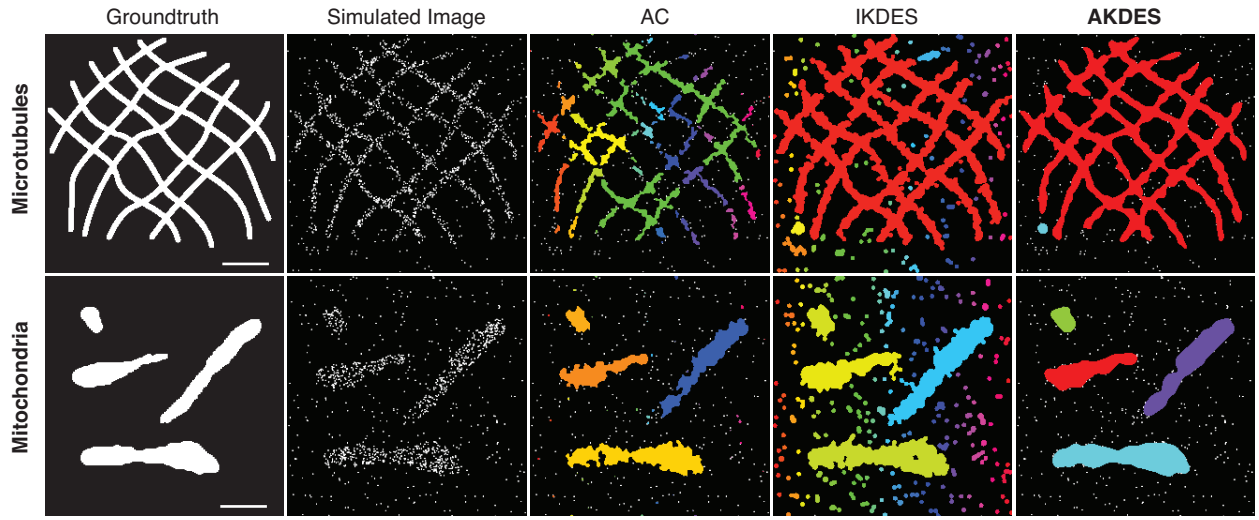

Figure 4.3: Comparison of different image segmentation approaches on simulated images. First column shoes the ground truth, second column shows the simulated SRLM images with SAR = 20 dB for microtubules and 10 dB for mitochondria, third column shows the Active Contour segmentation results, fourth column shows the isotropic kernel based segmentation results, and last column shows the proposed adaptive anisotropic kernel based segmentation results. The segmentation results are shown in random colors and overlapped on top of the simulated images. Scale bars, 500 nm.

local boundary direction and being robust to fluctuations resulted from the random distribution of activated fluorophores, and thus provided more accurate segmentation in both sample structures. We have also tested graph-cut based segmentation methods [58] and found the performance to be inferior to the proposed method (data not shown).

For quantitative comparison, we used the following segmentation evaluation metrics [59]: area similarity (AS) [60], which measures the goodness of segmentation compared to the ground truth, precision (P), which measures the ratio between the number of correctly segmented objects to the total number of segmented objects, and recall (R), which measures the ratio between the number of correctly segmented objects to the number of objects in the ground truth. The results are summarized in Table 4.1. All measures were averaged over all objects and all images. From the results, both AC and IKDES methods performed poorly because of over-segmentation and false segmentation. In contrast, our proposed method outperformed the other two by a large margin (10-fold improvement). The area similarly results also showed that the proposed method can correctly identify objects in both sample structures.

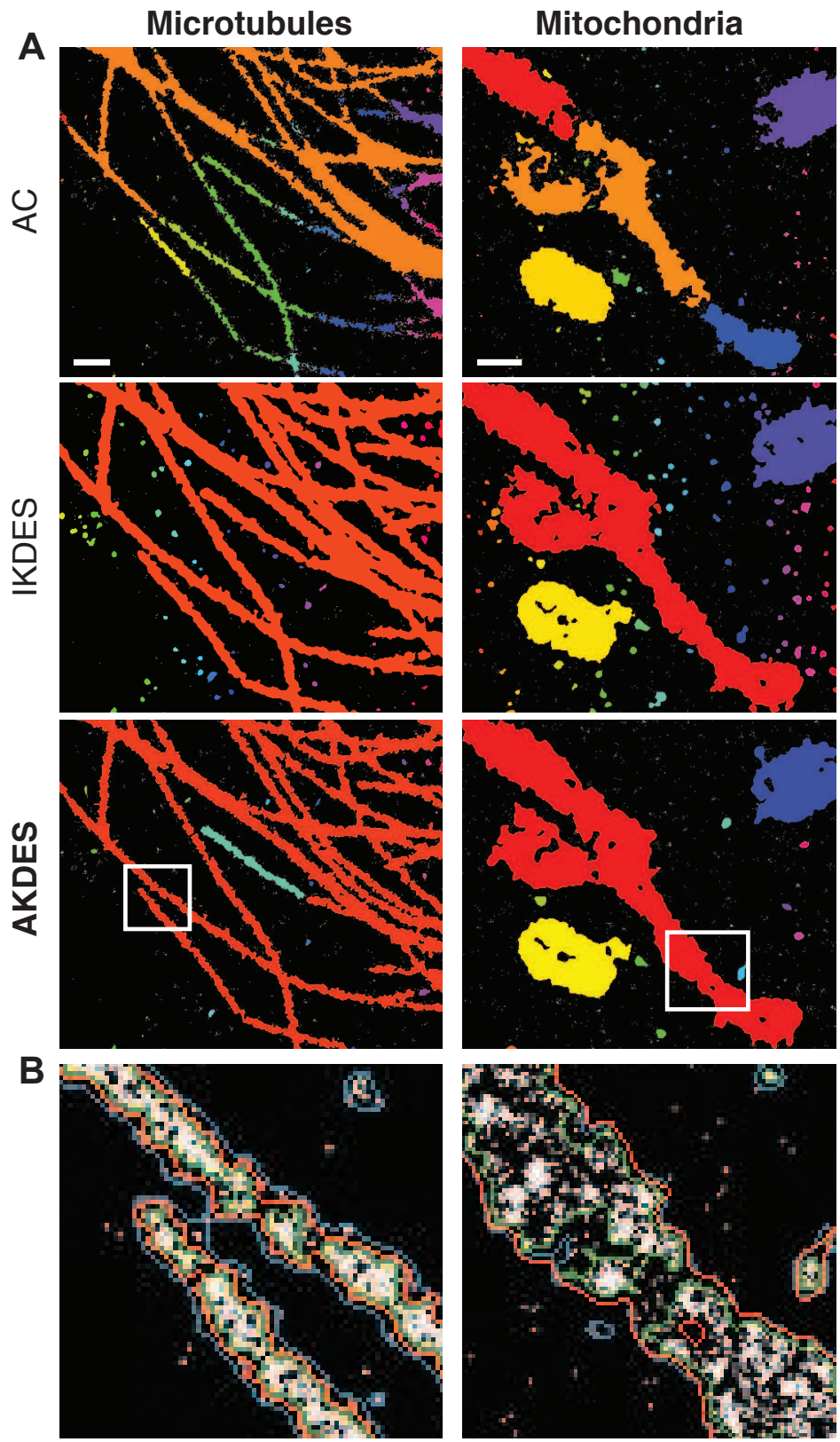

Figure 4.4: Real SRLM image segmentation results. (A) Comparison of different image segmentation approaches. (B) Comparison of segmentation contours in regions corresponding to the boxed regions in A, where green, blue, and red contours refer to AC, IKDES, and AKDES results, respectively. Scale bars, 500 nm.

	Microtubules			**Mitochondria**		
	AC	IKDES	**AKDES**	AC	IKDES	**AKDES**
AS	0.64	0.75	**0.79**	0.90	0.88	**0.90**
P	0.01	0.02	0.37	0.31	0.44	**0.96**
R	1.00	1.00	1.00	1.00	1.00	1.00

Table 4.1: Quantitative comparison of segmentation results of simulated data.

4.3.2 Real SRLM data

We further tested and compared these segmentation algorithms on real SRLM images of fluorescently labeled microtubules and mitochondria in fixed BS-C-1 cells imaged using a Nikon N-STORM system. Fig. 4.4 shows segmentation results in a region of ∼4,000×4,000 nm. The AC method again only captured fragmented clusters of particles while the IKDES method suffered from over-segmentation and false segmentation of the background artifacts (see Fig. 4.4B). In contrast, our proposed method captured better the boundary of the objects and was more robust to artifacts.

4.4 Summary

In this chapter, we present a simple density estimation based approach for segmentation of SRLM images. The proposed method uses an adaptive anisotropic kernel to estimate the underlying fluorophore density distribution, which can adjust the smoothing kernel according to the local spatial distribution. An empirically determined threshold is then used to segment the estimated density image. Experimental results showed that, compared to active contour method that was sensitive to the random boundary fluctuations and isotropic kernel based method that suffered from over-segmentation, the proposed method provided more reliable and accurate segmentation.

Chapter 5

Sliding-window Data Aggregation for Live Cell Imaging

Super resolution localization microscopy (SRLM) techniques such as STORM and PALM overcome the ∼200nm diffraction limit of conventional light microscopy by randomly activating separate fluorophores over time and computationally aggregating their nanometer resolution detected locations for image reconstruction. However, a basic limitation of current SRLM approaches for live cell imaging is their low temporal resolution due to motion blur, which arises if image objects move during image acquisition of the substantial number of raw images required for constructing the super-resolution image for a given time point. To overcome this limitation, we propose a sliding-window data aggregation method, which exploits the temporal correlation between the collected fluorescence images to achieve significantly higher frame rate and therefore better temporal resolution than current approaches. Specifically, images within a sliding window are aligned so that locations of detected fluorophores are aggregated to accelerate image reconstruction for higher temporal resolution. We tested and validated our method using both simulated and real live cell STORM image data.

5.1 Introduction

While many studies have demonstrated the capacity of SRLM to provide a nanoscale view into fixed cellular ultrastructures, current SRLM approaches for live cell imaging have only found limited

applications because of their low temporal resolution [61]. This is due to the fact that these approaches require a large number of raw images to be collected for reconstruction of a single SRLM image. To construct a SRLM movie (i.e., a sequence of SRLM images), a common practice is to pre-define a non-overlapped time window and to reconstruct individual SRLM image frame from those raw image frames of randomly activated fluorophores within each time window. The resulting SRLM image frame rates are often several folds slower than what conventional light microscopy can achieve. When imaging the dynamics of cellular structures such as the mitochondria show in Figure 5.1, longer image acquisition time per SRLM image frame leads to motion blur (see Figure 5.1A), which arises if image objects move while raw images are acquired for that SRLM image. On the other hand, to use a shorter image acquisition time is usually not an option because insufficient number of raw images will lead to poor quality of reconstructed images. This essentially leads to a *trade-off between the spatial and temporal resolution of SRLM* [62].

Current research that aims to address this trade-off between spatial and temporal resolution of the SRLM imaging mainly focuses on two strategies: 1) to use fast switching fluorophores and high-speed cameras, e.g. [63] and 2) to improve detection algorithms so that fluorophores of higher density can still be resolved, needing fewer frames for image reconstruction, e.g. [64–67]. Although these approaches have improved the temporal resolution of SRLM imaging to a certain degree (to approximately half a second per SRLM image), they all treat each SRLM image separately (Figure 5.2A) and focus on the reduction for the required acquisition time of each image without taking into account the fact that the location of fluorophores within consecutive images are interdependent both spatially and temporally.

In raw images, despite the randomness of photo-activation, the locations of the fluorophores are not completely random across the entire imaging region because they are samples of different parts of the same labeled object structures. While at each time step the detections are not sufficient to reconstruct cellular structures and to properly visualize image objects, the detections across longer range of time steps are correlated because they are samples of the same image object that is moving.

In this chapter, we exploit the temporal correlation between SRLM images to achieve significantly higher temporal resolution in live cell imaging using SRLM. Inspired from the concept of motion compensation used in video compression [68], we propose a data aggregation method. Specifically, we utilize the spatiotemporal interdependence of the detected fluorophores between successive raw images to estimate the underlying motion of the moving object. By utilizing a

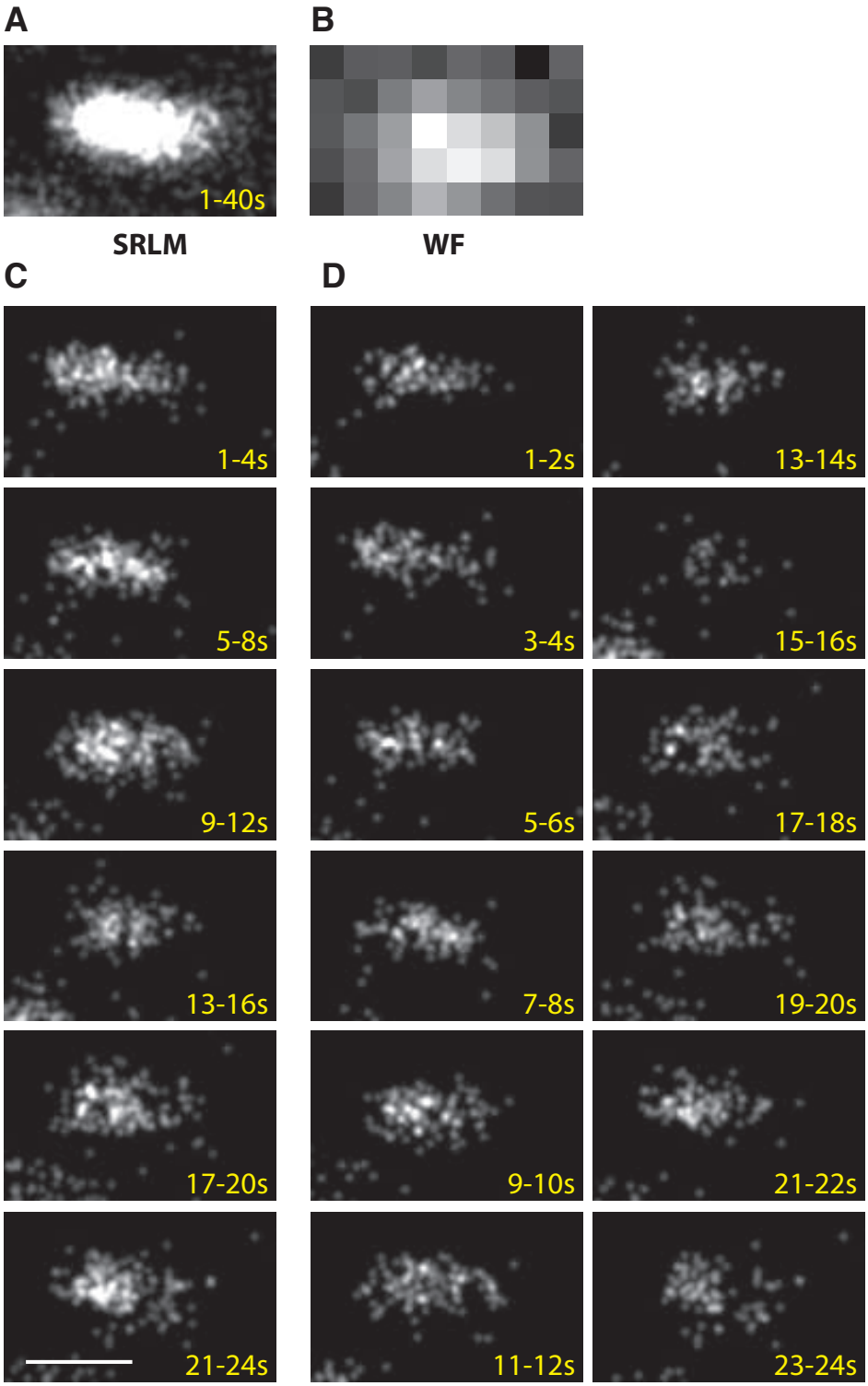

Figure 5.1: STORM images of a moving mitochondrion (moving towards right). (**A**) STORM image reconstructed from detected fluorophore positions over 40s. (**B**) A wide-field image before STORM imaging. (**C**) A sequence of STORM image frames reconstructed by setting the temporal resolution to one frame per 4 seconds. (**D**) Another sequence of STORM image frames reconstructed from the same fluorophore detections by setting the temporal resolution to one frame per 2 seconds. Scale bar, 500nm.

sliding-window scheme as shown in Figure 5.2B, the detected fluorophores confined within the window are aligned according to the estimated motion and combined into an SRLM image of the actual cellular structure. In this way, SRLM image reconstruction for live cell imaging becomes less restricted by motion blur so that higher frame rates can be achieved.

5.2 Methods

5.2.1 Problem Definition

Given is a time series of raw images, which can be divided into a set of time steps, $t_i, i = 1, 2, \ldots, T$. The time step size s_t can be determined according to the fluorophore density. By specifying a data aggregation time window h, an SRLM image is reconstructed by combining all localized fluorophores from the consecutive raw images within each time window h. The selection of h must be sufficiently large to reveal object structure as discussed in Chapter 3. When imaging a moving object, however, direct data aggregation will introduce motion blur, resulting in incorrect object structure. The goal here is to estimate the underlying motion of the image object to synthesis and reconstruct each SRLM image from the referencing frames. These referencing frames may be previous in time or even from the future.

Specifically, suppose each time step contains K raw images and a list of N_i localized fluorophores $p_{i,j} = [\mu_j, \upsilon_j]^\top, j = 1, 2, \ldots, N_i$, where μ_j and υ_j represent the spatial location where the fluorophore is localized. We assume that deformation of the moving objects is negligible within the time window h, which can be selected by observing the object, and that moving objects are spatially separated so that each moving object can be processed individually. Under these assumptions, we model the transformation between consecutive time steps as the rigid-body transformation

$$T_{\psi_i}(p) = \mathrm{R}_{\theta_i} p + [x_i, y_i]^\top,$$

where p is the variable in the spatial coordinate for the transform, R_{θ_i} is the rotation matrix and $\psi_i = (x_i, y_i, \theta_i)$ is the transformation parameter in which x_i and y_i are the relative spatial translations and θ_i is the rotation between the object's center of mass during the time step from t_i to t_{i+1}. This approach is applicable to deforming image objects as long as the deformation within the selected sliding window is negligible. By utilizing the image segmentation algorithm

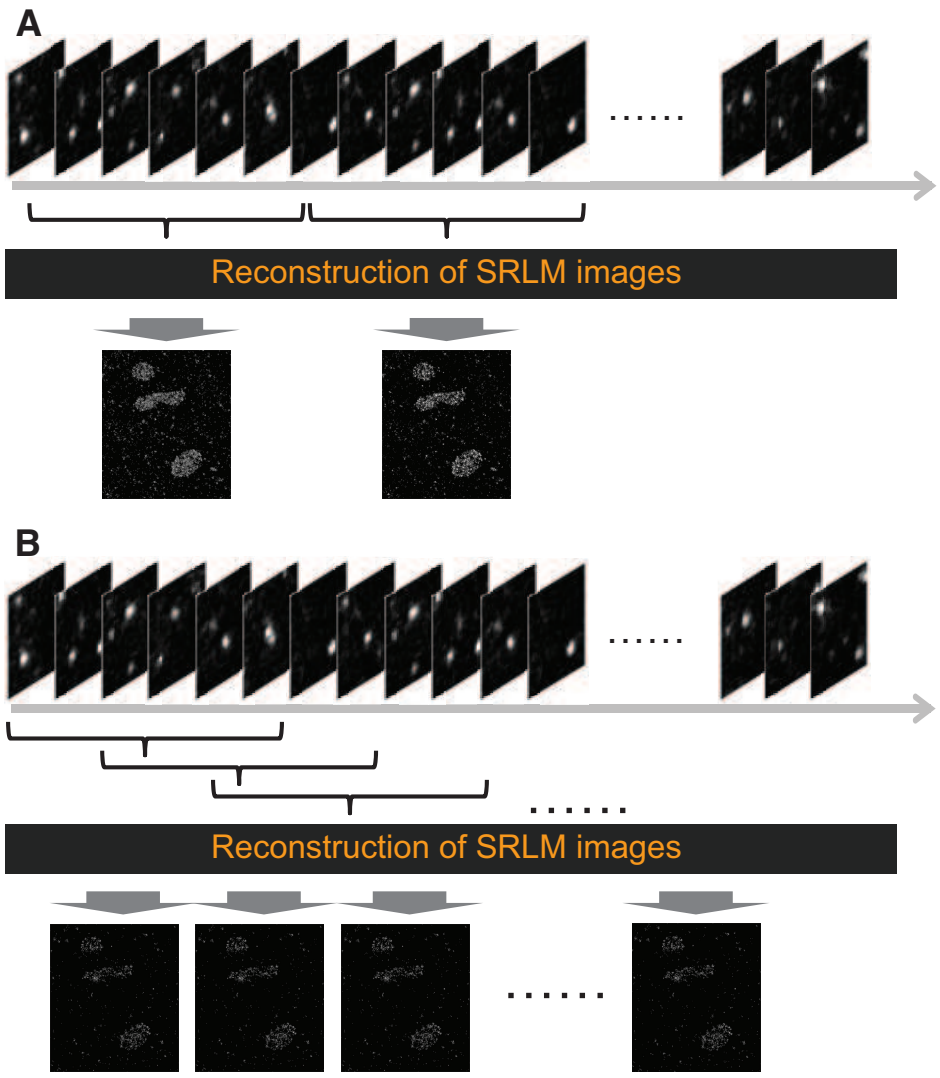

Figure 5.2: Comparison of current and proposed image reconstruction strategies. (**A**) Scheme of current non-overlapping window data aggregation method. (**B**) Scheme of the proposed sliding-window data aggregation method.

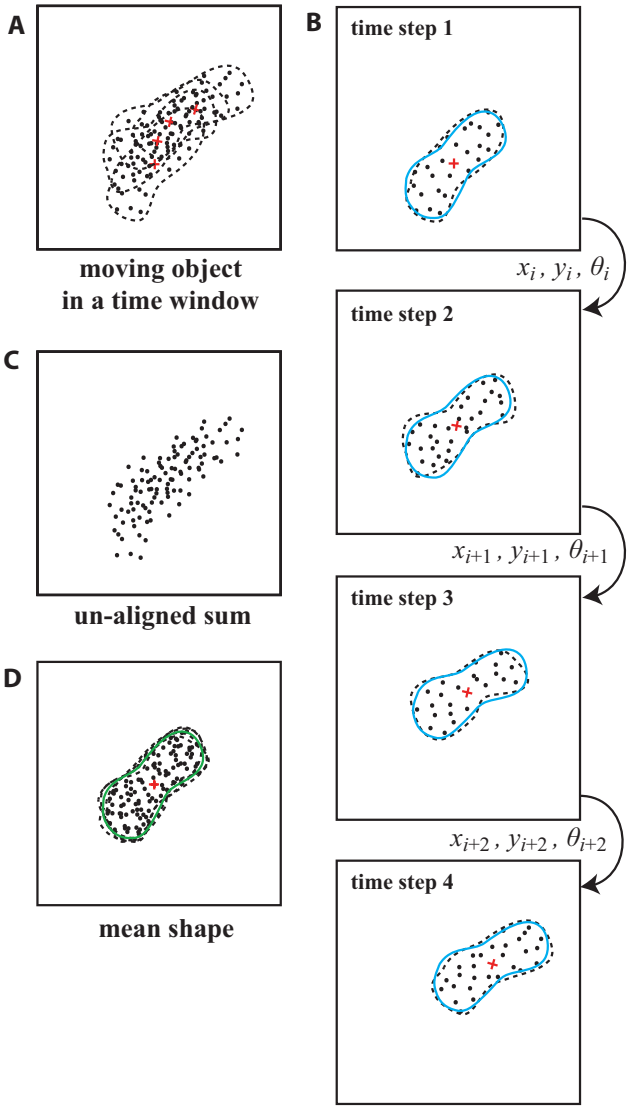

Figure 5.3: Live SRLM by motion and shape estimation. (**A**) A moving object within a time window. (**B**) A sequence of images of the moving object where at each time step, only a subset of random samples (dots) from the underlying true shape (blue solid line) is observed, from which the center of mass (red cross) and the shape (black dashed line) are estimated. (**C**) Current methods simply sum all time steps together without taking into account the motion, resulting in incorrect shape with motion blur. (**D**) The estimated shape (green colored outline) of the moving object matches well the true shape (blue colored outline) after the motion parameters x_i, y_i, θ_i are estimated and the fluorophores are aligned.

we developed previously [1], all raw images are firstly divided into several sub-regions containing single segmented object each. We can repeat the process for each successfully segmented region and combine the results.

5.2.2 Sliding-window Data Aggregation

For each time step t_i, we begin by preprocessing using approximate segmentation on the localized fluorophores of the moving object. The motion described by a sequence of transformations $\hat{T}_{\psi_i}$ is then estimated and the sliding-window aggregated SRLM images are consequently reconstructed through the following steps:

1. Estimate the transformation $\hat{T}_{\psi_i}$ between each pair of consecutive time steps (t_i and t_{i+1}) by finding the transformation parameters ψ_i between the segmentation of the localized fluorophores from the two time steps (See Figure 5.3C).

2. Repeat the process for all $t_i, i = 1, 2, \ldots, T$.

3. Specify a sliding-window of size h that is sufficient for the reconstructed image to reveal object structure and a sliding step size s that is sufficient for capturing the object dynamics.

4. Align the fluorophores from the time steps t to $t + h$, where h is the time window that is sufficient for the reconstructed image to reveal object structure.

5.2.3 Motion Estimation

Given two subsets of the localized fluorophores of the same moving object from the consecutive time steps, our goal is to estimate the relative motion, including displacement and rotation, between them. Based on our non-deformable object assumption, this problem can be reformulated as finding the rigid transformation between two sets of the localized fluorophores in the consecutive time steps. While one way would be to apply image registration such as correlation or mutual-information based methods, we found from our experiments that these approaches performed poorly, likely due to the sparsity and randomness of the localized fluorophores. We thus propose two simple but more robust approaches: 1) finding the centroid of the detected fluorophores and the major orientation using the spatial principle component analysis and 2) finding the center of mass of the detected fluorophore-covered area and its major orientation. In either approach, we can use the centroid

and major orientation to estimate the rigid transformation from one set to the other set of the fluorophores.

5.3 Results

To evaluate the proposed method, we performed experiments on both simulated and real SRLM images of live mitochondria.

5.3.1 Simulated Data

We generated the simulated data using a sequence of raw images (100,000 frames) of mitochondria fluorescently labeled using Alexa 488 from fixed BS-C-1 cells imaged using a Nikon N-STORM microscope. The fluorophores were detected (∼10,000 fluorophores) using the software described in [65]. A curvilinear motion of a moving distance ∼800nm was generated artificially to simulate the movement of mitochondria (the black dotted line shown in Figure 5.4A, C). The collected fluorophores were divided into 25 time steps and the proposed methods were applied to estimate the motions. To reduce the variability due to the randomness of the fluorophores, we smoothed the estimated motion using a Gaussian filter with $\sigma = 5$. From the results shown in Figure 5.4A-D, we can see that the error is very small in the beginning steps and gradually increases, likely due to the degradation of the fluorophore signals, a limitation of the simulated image data. Overall, however, the error is below 40nm. Next, we chose a sliding window of size 60,000 frames with a sliding step size of 1,000 frames to reconstruct SRLM images. Figure 5.4E shows the comparison of sliding-window based reconstructed SRLM images between aligned and unaligned fluorophore detections with respect to the ground truth after applying the segmentation algorithm described in [1] for extracting mitochondrial structures. As expected, the aligned one matches well with the ground truth with the mean boundary error significantly reduced compared with the unaligned one (See Figure 5.4F). With the sliding step size of 1,000 frames, the proposed method accelerated the frame rate significantly by thirty-folds (originally 30,000 frames are required to reliably reveal the structure) to capture the motion (∼8nm, which is smaller than the reconstructed SRLM image pixel size of 10nm).

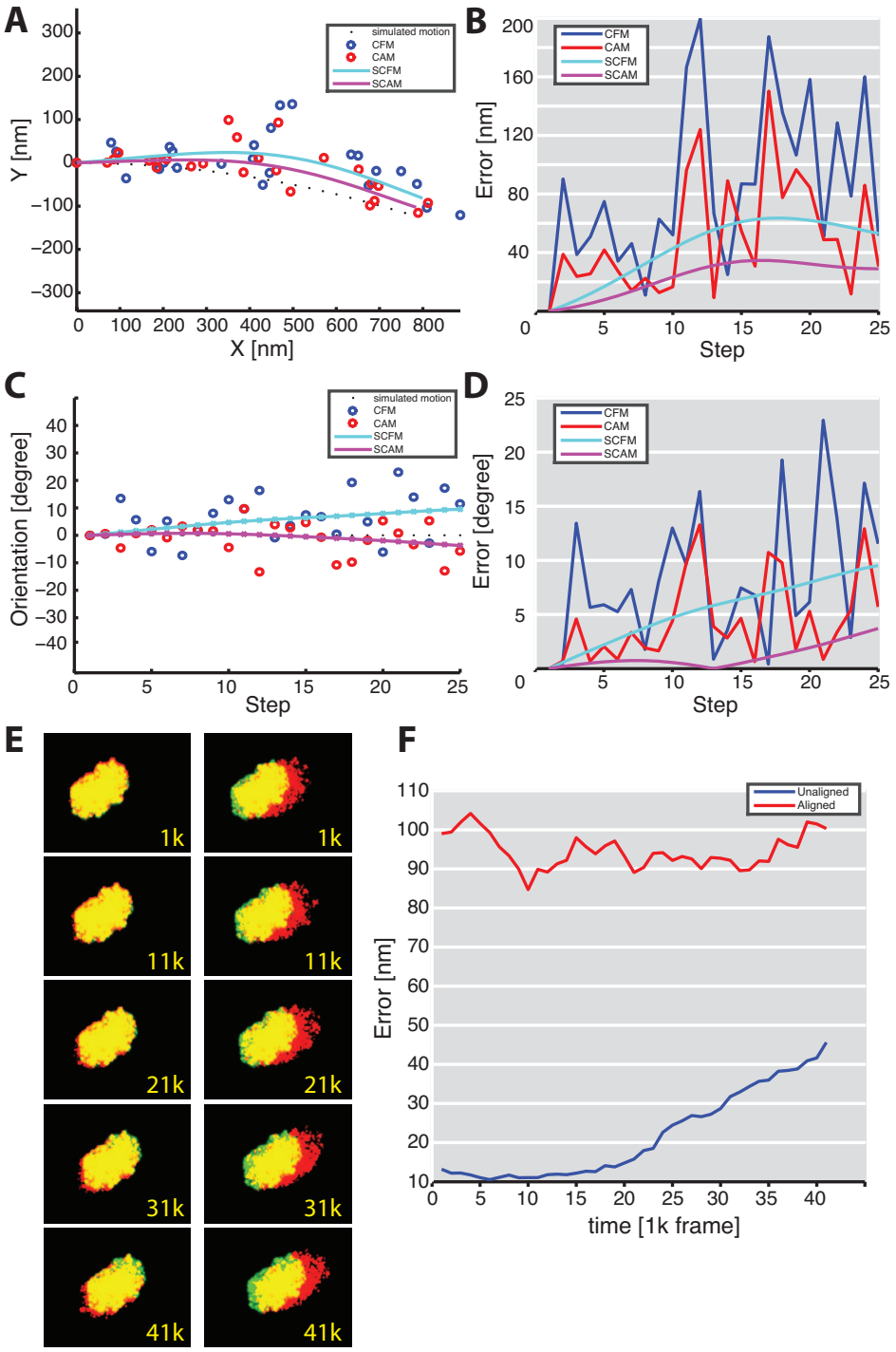

Figure 5.4: Motion estimation from SRLM images of fixed mitochondria with simulated motion. (**A**, **C**) The trajectory and the orientation of the simulated motion shown as black dotted line, the motion estimated by the centroids of the detected fluorophores (CFM) shown as blue circles, the motion estimated by the center of mass of the fluorophore-covered area (CAM) shown as red circles, and the motion estimations after smoothing for both methods (SCFM and SCAM) shown as cyan and purple lines, respectively. (**B**, **D**) The error of the estimated motions for both methods (blue and red lines, respectively) and the ones after smoothing (cyan and purple line, respectively). (**E**) The SRLM image frames reconstructed after the detected fluorophores are aligned (red colored channel) overlapped with the ground truth (green colored channel) on the left column and the SRLM image frames reconstructed before the detected fluorophores are aligned (red colored channel) overlapped with the ground truth (green colored channel) on the right column. The matched area is shown in yellow. (**F**) The mean boundary error of the segmentation of mitochondria from SRLM image frames before and after the detected fluorophores are aligned (red and blue lines respectively) compared to the ground truth.

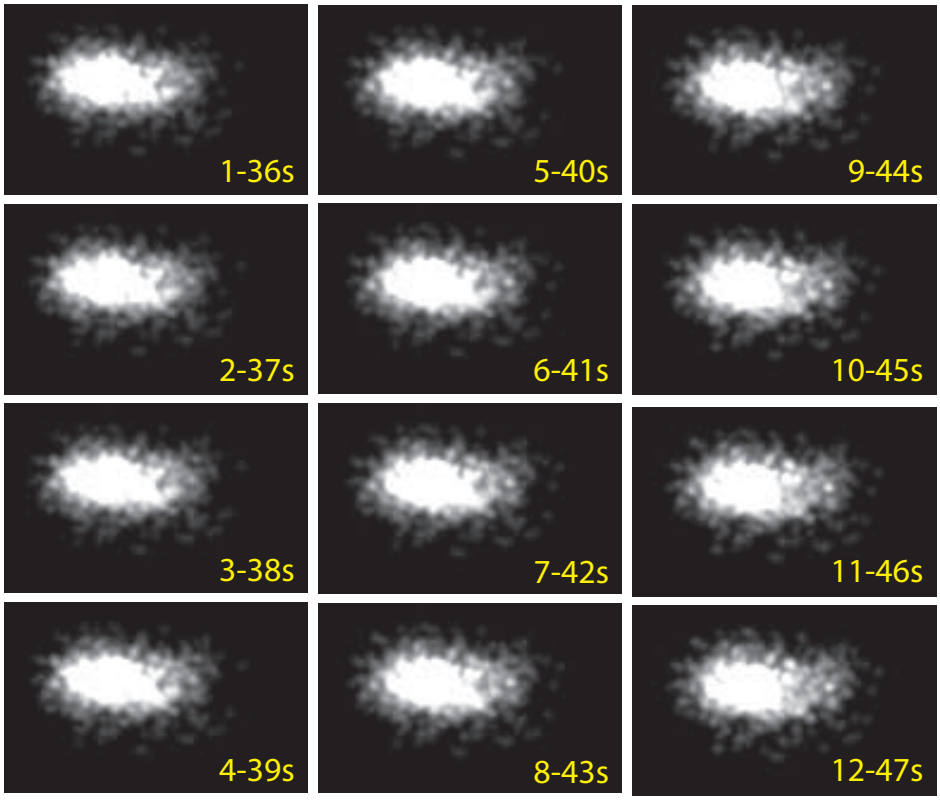

Figure 5.5: Result of data aggregated SRLM images reconstructed with aligned fluorophore detections. The frame rate is 1 frame per second.

5.3.2 Real SRLM Data of Live Cells

We further tested our method on actual SRLM images of mitochondria fluorescently labeled using MitoTracker Red in live BS-C-1 cells. The SRLM images were collected using a Nikon N-STORM microscope. Figure 5.5 shows the sliding window aggregated results using aligned fluorophore detections in a region of ∼800×1280nm. Compared to the existing approaches that use nonoverlapping aggregation (See Figure 5.1D, the frame rate is 0.5 frame per second), the proposed method reveals the structure of the mitochondrion with higher frame rate of 1 frame per second, which represents a doubling of temporal resolution.

5.4 Discussion

With exactly the same data, our proposed method works by interring the underlying hidden motion information and taking prior knowledge of the motion into account to estimate and synthesis missing images. The limitation of this method lies to the selection of the time step size and the sliding

window size. The time step size controls directly to the performance of the motion estimation. While a larger time step size is desired to yield accurate motion estimation, the assumption of rigid body transformation, i.e., the object did not deform or even move within this time step, fundamentally sets a limit of the maximum value of the time step size. The sliding window size, on the other hand, has to fall inside a similar but less restrict requirement that the object may move but cannot deform within the sliding window.

Under such requirement, the proposed method shows great potential for following biological image analyses, for example, object tracking or spatiotemporal distribution characterization.

5.5 Summary

In this chapter, we present a sliding window based data aggregation method for improving the temporal resolution of SRLM for live cell imaging. By aligning detected fluorophores of different frames within the sliding window, we aggregate the fluorophore locations to achieve accelerated image reconstruction while avoiding the motion blur. Experimental results show that our method significantly reduces the trade-off between spatial and temporal resolution of SRLM imaging. In addition, the proposed method can be combined with existing strategies such as using faster switching fluorophores or high-speed cameras for improvement of temporal resolution.

Chapter 6

Conclusions and Future Works

6.1 Conclusions

In this thesis, we have presented a computational toolbox for super-resolution localization microscopy image analysis including the following three main techniques:

1. **An image quality assessment method for SRLM images**. The proposed method presented in Chapter 3 provides a new image quality measure for directly quantifying the image information to determine whether the imaging length is sufficient to reveal the structure of imaging objects.

2. **A kernel density-based image segmentation algorithm**. We presented in Chapter 4 a new image segmentation method specifically designed for SRLM images based on kernel density estimation. Our results show that the proposed method is capabile of adapting the kernel to segment structures from images reliably and accurately.

3. **A sliding-window based data aggregation method**. In Chapter 5, we present a novel framework of data aggregation to enable SRLM image analysis of live cells with improved temporal resolution. Our results show that the proposed method can improve the temporal resolution by 2 folds. The propose method can also be combined with other approaches of improved fluorophores or equipments to further empower the SRLM imaging.

6.2 Future Works

We have several directions planned for future work. For image analysis of SRLM images, we would like to expand the proposed segmentation algorithm to work under multiresolution framework, which could not only greatly improve the run-time speed but also reveal different morphologies of the structures in different scales. In addition, for precise quantification of the structures, the physical properties of fluorescence probes must be considered, for example the length of primary/secondary antibody, which increase the effective size of the probe. We would like to incorporate this into the density estimation of fluorophore distribution to reveal the underly labeling object. Furthermore, the proposed methods can be extended to directly work on the raw image data without extra localization process. Finally, we would also like to expand the proposed SRLM image analysis tool for developing more functions designed for different cellular structures.

Bibliography

[1] K.-C. J. Chen, G. Yang, and J. Kovačević, "Spatial density estimation based segmentation of super-resolution localization microscopy images," in *Proc. IEEE Int. Conf. Image Process.*, Paris, Oct. 2014.

[2] S. T. Hess, T. P. Girirajan, and M. D. Mason, "Ultra-High Resolution Imaging by Fluorescence Photoactivation Localization Microscopy," *Biophysical Journal*, vol. 91, no. 11, pp. 4258–4272, dec 2006.

[3] N. Banterle, K. H. Bui, E. a. Lemke, and M. Beck, "Fourier ring correlation as a resolution criterion for super-resolution microscopy." *Journal of structural biology*, vol. 183, no. 3, pp. 363–7, sep 2013.

[4] R. P. J. Nieuwenhuizen, K. A. Lidke, M. Bates, D. L. Puig, D. Grünwald, S. Stallinga, and B. Rieger, "Measuring image resolution in optical nanoscopy," *Nature methods*, vol. 10, no. 6, pp. 557–62, jun 2013.

[5] E. Betzig, G. H. Patterson, R. Sougrat, O. W. Lindwasser, S. Olenych, J. S. Bonifacino, M. W. Davidson, J. Lippincott-Schwartz, and H. F. Hess, "Imaging Intracellular Fluorescent Proteins at Nanometer Resolution," *Science*, vol. 313, no. 5793, pp. 1642–1645, sep 2006.

[6] M. G. L. Gustafsson, "Nonlinear structured-illumination microscopy: Wide-field fluorescence imaging with theoretically unlimited resolution," *Proceedings of the National Academy of Sciences*, vol. 102, no. 37, pp. 13 081–13 086, sep 2005.

[7] S. W. Hell, "Far-Field Optical Nanoscopy," *Science*, vol. 316, no. 5828, pp. 1153–1158, may 2007.

[8] M. J. Rust, M. Bates, and X. Zhuang, "Sub-diffraction-limit imaging by stochastic optical reconstruction microscopy (STORM)," *Nature methods*, vol. 3, no. 10, pp. 793–5, oct 2006.

[9] K. Xu, G. Zhong, and X. Zhuang, "Actin, spectrin, and associated proteins form a periodic cytoskeletal structure in axons." *Science*, vol. 339, no. 6118, pp. 452–6, jan 2013.

[10] S.-H. Shim, C. Xia, G. Zhong, H. P. Babcock, J. C. Vaughan, B. Huang, X. Wang, C. Xu, G.-Q. Bi, and X. Zhuang, "Super-resolution fluorescence imaging of organelles in live cells with photoswitchable membrane probes." *Proceedings of the National Academy of Sciences of the United States of America*, vol. 109, no. 35, pp. 13 978–83, aug 2012.

[11] T. J. Gould, S. T. Hess, and J. Bewersdorf, "Optical nanoscopy: from acquisition to analysis." *Annual review of biomedical engineering*, vol. 14, pp. 231–54, jan 2012.

[12] B. Huang, M. Bates, and X. Zhuang, "Super-Resolution Fluorescence Microscopy," *Annual Review of Biochemistry*, vol. 78, no. 1, pp. 993–1016, jun 2009.

[13] D. Baddeley, M. B. Cannell, and C. Soeller, "Visualization of localization microscopy data." *Microscopy and microanalysis*, vol. 16, no. 1, pp. 64–72, feb 2010.

[14] S. Herbert, H. Soares, C. Zimmer, and R. Henriques, "Single-molecule localization super-resolution microscopy: deeper and faster." *Microscopy and microanalysis*, vol. 18, no. 6, pp. 1419–29, dec 2012.

[15] K.-C. J. Chen, J. Kovačević, and G. Yang, "Structure-based determination of imaging length for super-resolution localization microscopy," in *Proc. IEEE Int. Symp. Biomed. Imag.*, Beijing, Apr. 2014, pp. 991–994.

[16] K.-C. J. Chen, J. M. Szymanski, A. W. Feinberg, J. Kovačević, and G. Yang, "Density-based quality assessment of reconstructed images for super-resolution localization microscopy," *Nature Methods*, 2015.

[17] K.-C. J. Chen, Y. Yu, J. Kovačević, and G. Yang, "A sliding-window data aggregation method for super-resolution imaging of live cells," in *Proc. IEEE Int. Symp. Biomed. Imag.*, Brooklyn, NY, Apr. 2015.

[18] *Principles of optics: electromagnetic theory of propagation, interference and diffraction of light.*

[19] M. G. L. Gustafsson, "Surpassing the lateral resolution limit by a factor of two using structured illumination microscopy. SHORT COMMUNICATION," *Journal of Microscopy*, vol. 198, no. 2, pp. 82–87, may 2000.

[20] R. E. Thompson, D. R. Larson, and W. W. Webb, "Precise nanometer localization analysis for individual fluorescent probes." *Biophysical journal*, vol. 82, no. 5, pp. 2775–83, may 2002.

[21] S. Wolter, A. Löschberger, T. Holm, S. Aufmkolk, M.-C. Dabauvalle, S. van de Linde, and M. Sauer, "rapidSTORM: accurate, fast open-source software for localization microscopy." *Nature methods*, vol. 9, no. 11, pp. 1040–1, nov 2012.

[22] A. R. Small and R. Parthasarathy, "Superresolution Localization Methods." *Annual review of physical chemistry*, no. November 2013, pp. 107–125, nov 2013.

[23] E. J. Rees, M. Erdelyi, G. S. K. Schierle, A. Knight, and C. F. Kaminski, "Elements of image processing in localization microscopy," *Journal of Optics*, vol. 15, no. 9, p. 094012, sep 2013.

[24] L. Zhu, W. Zhang, D. Elnatan, and B. Huang, "Faster STORM using compressed sensing." *Nature methods*, vol. 9, no. 7, pp. 721–3, jul 2012.

[25] S. J. Holden, S. Uphoff, and A. N. Kapanidis, "DAOSTORM: an algorithm for high- density super-resolution microscopy." *Nature methods*, vol. 8, no. 4, pp. 279–80, apr 2011.

[26] F. Grull, M. Kirchgessner, R. Kaufmann, M. Hausmann, and U. Kebschull, "Accelerating Image Analysis for Localization Microscopy with FPGAs," in *2011 21st International Conference on Field Programmable Logic and Applications*. IEEE, sep 2011, pp. 1–5.

[27] S. M. Anthony and S. Granick, "Image Analysis with Rapid and Accurate Two-Dimensional Gaussian Fitting," *Langmuir*, vol. 25, no. 14, pp. 8152–8160, jul 2009.

[28] C. S. Smith, N. Joseph, B. Rieger, and K. a. Lidke, "Fast, single-molecule localization that achieves theoretically minimum uncertainty." *Nature methods*, vol. 7, no. 5, pp. 373–5, may 2010.

[29] N. Brede and M. Lakadamyali, "GraspJ - An Open Source, Real-Time Analysis Package for Super-Resolution Imaging," *Biophysical Journal*, vol. 102, no. 3, p. 724a, jan 2012.

[30] R. Starr, S. Stahlheber, and A. Small, "Fast maximum likelihood algorithm for localization of fluorescent molecules: erratum," *Optics Letters*, vol. 37, no. 11, p. 1967, jun 2012.

[31] L. Niu and J. Yu, "Investigating intracellular dynamics of FtsZ cytoskeleton with photoactivation single-molecule tracking." *Biophysical journal*, vol. 95, no. 4, pp. 2009–16, aug 2008.

[32] D. Baddeley, M. B. Cannell, and C. Soeller, "Three-dimensional sub-100 nm super-resolution imaging of biological samples using a phase ramp in the objective pupil," *Nano Research*, vol. 4, no. 6, pp. 589–598, jun 2011.

[33] R. Henriques, M. Lelek, E. F. Fornasiero, F. Valtorta, C. Zimmer, and M. M. Mhlanga, "QuickPALM: 3D real-time photoactivation nanoscopy image processing in ImageJ," *Nature Methods*, vol. 7, no. 5, pp. 339–340, may 2010.

[34] R. Parthasarathy, "Rapid, accurate particle tracking by calculation of radial symmetry centers." *Nature methods*, vol. 9, no. 7, pp. 724–6, jul 2012.

[35] P. Křížek, I. Raška, and G. M. Hagen, "Minimizing detection errors in single molecule localization microscopy." *Optics express*, vol. 19, no. 4, pp. 3226–35, feb 2011.

[36] S. B. Andersson, "Localization of a fluorescent source without numerical fitting." *Optics express*, vol. 16, no. 23, pp. 18 714–24, nov 2008.

[37] K. I. Mortensen, L. S. Churchman, J. a. Spudich, and H. Flyvbjerg, "Optimized localization analysis for single-molecule tracking and super-resolution microscopy," *Nature Methods*, vol. 7, no. 5, pp. 377–381, may 2010.

[38] M. J. Mlodzianoski, J. M. Schreiner, S. P. Callahan, K. Smolková, A. Dlasková, J. Šantorová, P. Ježek, and J. Bewersdorf, "Sample drift correction in 3D fluorescence photoactivation localization microscopy," *Optics Express*, vol. 19, no. 16, p. 15009, aug 2011.

[39] C. Coltharp, X. Yang, and J. Xiao, "Quantitative analysis of single-molecule superresolution images," *Current Opinion in Structural Biology*, vol. 28, pp. 112–121, oct 2014.

[40] S. L. Veatch, B. B. Machta, S. a. Shelby, E. N. Chiang, D. a. Holowka, and B. a. Baird, "Correlation functions quantify super-resolution images and estimate apparent clustering due to over-counting." *PloS one*, vol. 7, no. 2, p. e31457, jan 2012.

[41] P. Sengupta and J. Lippincott-Schwartz, "Quantitative analysis of photoactivated localization microscopy (PALM) datasets using pair-correlation analysis." *BioEssays : news and reviews in molecular, cellular and developmental biology*, vol. 34, no. 5, pp. 396–405, may 2012.

[42] P. Sengupta, T. Jovanovic-Talisman, and J. Lippincott-Schwartz, "Quantifying spatial organization in point-localization superresolution images using pair correlation analysis." *Nature protocols*, vol. 8, no. 2, pp. 345–54, feb 2013.

[43] M. Bates, B. Huang, G. T. Dempsey, and X. Zhuang, "Multicolor super-resolution imaging with photo-switchable fluorescent probes." *Science*, vol. 317, no. 5845, pp. 1749–53, sep 2007.

[44] A. Dani, B. Huang, J. Bergan, C. Dulac, and X. Zhuang, "Superresolution imaging of chemical synapses in the brain." *Neuron*, vol. 68, no. 5, pp. 843–56, dec 2010.

[45] S. Maji and M. P. Bruchez, "Inferring biological structures from super-resolution single molecule images using generative models." *PloS one*, vol. 7, no. 5, p. e36973, jan 2012.

[46] N. Dalal and B. Triggs, "Histograms of Oriented Gradients for Human Detection," in *2005 IEEE Computer Society Conference on Computer Vision and Pattern Recognition (CVPR'05)*, vol. 1. IEEE, 2005, pp. 886–893.

[47] J. Daugman, "Complete discrete 2-D Gabor transforms by neural networks for image analysis and compression," *IEEE Transactions on Acoustics, Speech, and Signal Processing*, vol. 36, no. 7, pp. 1169–1179, jul 1988.

[48] B. Efron and R. J. Tibshirani, *An Introduction to the Bootstrap*, 1994.

[49] L. Wasserman, *All of Nonparametric Statistics*, ser. Springer Texts in Statistics. New York, NY: Springer New York, 2006.

[50] D. Mattes, D. R. Haynor, H. Vesselle, T. K. Lewellyn, and W. Eubank, "Nonrigid multimodality image registration," in *Medical . . .*, vol. 4322, 2001, pp. 1609–1620.

[51] Y. Boykov and G. Funka-Lea, "Graph Cuts and Efficient N-D Image Segmentation," *International Journal of Computer Vision*, vol. 70, no. 2, pp. 109–131, nov 2006.

[52] M. Kass, A. Witkin, and D. Terzopoulos, "Snakes: Active contour models," *International Journal of Computer Vision*, vol. 1, no. 4, pp. 321–331, jan 1988.

[53] T. F. Chan and L. A. Vese, "Active contours without edges." *IEEE transactions on image processing : a publication of the IEEE Signal Processing Society*, vol. 10, no. 2, pp. 266–77, jan 2001.

[54] L. Vese and T. Chan, "A multiphase level set framework for image segmentation using the Mumford and Shah model," *International journal of computer vision*, vol. 50, no. 3, pp. 271–293, 2002.

[55] G. Srinivasa, M. C. Fickus, Y. Guo, A. D. Linstedt, and J. Kovacević, "Active mask segmentation of fluorescence microscope images," *IEEE Trans Image Processing*, vol. 18, no. 8, pp. 1817–29, aug 2009.

[56] D. W. Scott, Ed., *Multivariate Density Estimation*, ser. Wiley Series in Probability and Statistics. Hoboken, NJ, USA: John Wiley & Sons, Inc., aug 1992.

[57] B. Silverman, *Density Estimation for Statistics and Data Analysis*. London: Chapman & Hall, 1986.

[58] Y. Boykov and V. Kolmogorov, "An experimental comparison of min-cut/max-flow algorithms for energy minimization in vision." *IEEE transactions on pattern analysis and machine intelligence*, vol. 26, no. 9, pp. 1124–37, sep 2004.

[59] K.-C. J. Chen, Y. Yu, R. Li, H.-C. Lee, G. Yang, and J. Kovačević, "Adaptive active-mask image segmentation for quantitative characterization of mitochondrial morphology," in *Proc. IEEE Int. Conf. Image Process.*, Orlando, FL, Sep. 2012, pp. 2033–2036.

[60] A. P. Zijdenbos, B. M. Dawant, R. A. Margolin, and A. C. Palmer, "Morphometric analysis of white matter lesions in MR images: Method and validation," *IEEE Trans. Med. Imag.*, vol. 13, pp. 716 – 724, Dec. 1994.

[61] D. Kamiyama and B. Huang, "Development in the STORM." *Developmental cell*, vol. 23, no. 6, pp. 1103–10, dec 2012.

[62] H. Shroff, C. G. Galbraith, J. A. Galbraith, and E. Betzig, "Live-cell photoactivated localization microscopy of nanoscale adhesion dynamics." *Nature methods*, vol. 5, no. 5, pp. 417–23, may 2008.

[63] G. T. Dempsey, J. C. Vaughan, K. H. Chen, M. Bates, and X. Zhuang, "Evaluation of fluorophores for optimal performance in localization-based super-resolution imaging." *Nature methods*, vol. 8, no. 12, pp. 1027–36, dec 2011.

[64] T. Quan, H. Zhu, X. Liu, Y. Liu, J. Ding, S. Zeng, and Z.-L. Huang, "High-density localization of active molecules using Structured Sparse Model and Bayesian Information Criterion." *Optics express*, vol. 19, no. 18, pp. 16 963–74, aug 2011.

[65] H. Babcock, Y. M. Sigal, and X. Zhuang, "A high-density 3D localization algorithm for stochastic optical reconstruction microscopy," *Optical Nanoscopy*, vol. 1, no. 1, p. 6, 2012.

[66] S. Cox, E. Rosten, J. Monypenny, T. Jovanovic-Talisman, D. T. Burnette, J. Lippincott-Schwartz, G. E. Jones, and R. Heintzmann, "Bayesian localization microscopy reveals nanoscale podosome dynamics." *Nature methods*, vol. 9, no. 2, pp. 195–200, mar 2012.

[67] H. P. Babcock, J. R. Moffitt, Y. Cao, and X. Zhuang, "Fast compressed sensing analysis for super-resolution imaging using L1-homotopy," *Optics Express*, vol. 21, no. 23, p. 28583, nov 2013.

[68] Haibo Li, A. Lundmark, and R. Forchheimer, "Image sequence coding at very low bit rates: a review," *IEEE Transactions on Image Processing*, vol. 3, no. 5, pp. 589–609, 1994.